crystals

MDPI

Article

Structural and Mechanical Properties of Y_2SiO_5-Lu_2SiO_5 Solid Solutions from *Ab Initio* Calculations

Alexander Platonenko [1], Marina Konuhova [1], Dmitry V. Bocharov [1,2,*] and Anatoli I. Popov [1,*]

[1] Institute of Solid State Physics, University of Latvia, 8 Kengaraga Str., LV-1063 Riga, Latvia; a.platonenko@cfi.lu.lv (A.P.); marina.konuhova@cfi.lu.lv (M.K.)
[2] Transport and Telecommunication Institute, Engineering Faculty, 2 Lauvas Str., LV-1019 Riga, Latvia
* Correspondence: bocharov@cfi.lu.lv (D.V.B.); popov@cfi.lu.lv (A.I.P.)

Abstract

Y_2SiO_5 (YSO) and Lu_2SiO_5 (LSO) are orthosilicates used in photonic and scintillation applications. Isovalent substitution on the rare-earth sublattice in YSO–LSO solid solutions enables systematic tuning of lattice parameters and elastic properties without changing the underlying monoclinic structural framework. A systematic *ab initio* study of structural, elastic, and vibrational properties of Ce-free YSO–LSO solid solutions is performed within density functional theory using a localized Gaussian-type orbital basis. Nine compositions spanning the full range from YSO to LSO with a Lu content step of 12.5% are investigated. A total of 76 symmetry-independent Y/Lu substitution patterns are explicitly constructed. For each configuration, full geometry optimization and calculation of second-order elastic constants are carried out using the stress–strain approach. Bulk, shear, and Young's moduli, as well as Poisson's ratio, are obtained using the Voigt, Reuss, and Hill averaging schemes. Sound velocities and Debye temperatures are derived from the Hill-averaged elastic moduli and density. The unit-cell volumes decrease smoothly with increasing Lu content and follow Vegard's law, indicating uniform lattice contraction. The Hill-averaged bulk modulus increases from 92 GPa (YSO) to 115 GPa (LSO), the Young's modulus rises from 151 to 180 GPa, and a strong directional anisotropy (ratio ∼2) is preserved across the entire series. The Debye temperature decreases monotonically from 518 K to 439 K, indicating that the increase in mass density outweighs the stiffening-induced tendency toward higher sound velocities. These results provide quantitative guidance for composition selection and stress management in LYSO-based crystal detectors.

Keywords: orthosilicates; solid solutions; scintillators; mechanical properties; *ab initio*

Check for updates

Academic Editor: Daisuke Nakauchi

Received: 11 March 2026
Revised: 13 May 2026
Accepted: 25 May 2026
Published: 4 June 2026

Copyright: © 2026 by the authors. Licensee MDPI, Basel, Switzerland. This article is an open access article distributed under the terms and conditions of the Creative Commons Attribution (CC BY) license.

1. Introduction

Scintillator materials emit light when exposed to ionizing radiation. This property makes them indispensable in diverse applications that include medical diagnostics, radiation detection, security, industrial inspection, and a wide range of scientific research methods [1–9].

Scintillation crystals are essential components of electromagnetic calorimeters in high-energy physics; for example, $PbWO_4$ crystals are used in the Compact Muon Solenoid (CMS) electromagnetic calorimeter at the Large Hadron Collider (LHC) [10,11]. More broadly, scintillator research includes tungstates, halides, garnets, oxyorthosilicates, and related wide-band-gap materials [12–20].

Y_2SiO_5 (YSO) is a scintillator host material used in photonic and radiation-detection applications [21,22]. Its rare-earth sublattice can be progressively modified by replacing Y^{3+} with Lu^{3+}, giving the solid-solution family $(Lu_xY_{1-x})_2SiO_5$, hereafter denoted as LYSO. Complete replacement of Y by Lu gives the Lu-rich end member Lu_2SiO_5 (LSO) [23,24].

LYSO, a solid solution of LSO and YSO, retains the advantageous growth characteristics of YSO and the desirable scintillating properties of LSO. This provides several advantages, including a lower melting point, reduced raw material costs, and easier incorporation of cerium activators into the crystal structure. Furthermore, the incorporation of Lu into the YSO lattice substantially increases the density and effective atomic number relative to pure YSO, thereby improving the stopping power, while still retaining more favorable growth characteristics and lower cost than pure LSO [25,26].

Importantly, although the present study addresses the intrinsic Ce-free host lattice, its properties are directly relevant for experimentally realized LYSO-based scintillators, where mechanical stability governs crystal growth, machining, and long-term device reliability. Therefore, a brief overview of scintillation applications is retained here to connect the fundamental description of the host matrix with its practical use and to ensure that the manuscript remains accessible to both theoretical and experimental audiences. LYSO scintillators, doped with cerium (Ce), have become essential in applications such as medical imaging and high-energy physics due to their high stopping power, fast decay time, and high light output [2,3]. The development of LYSO was initially driven by the demand for improved performance in positron emission tomography (PET) systems, where its high density and effective atomic number make it an ideal material for efficient radiation detection [2,4]. LYSO is non-hygroscopic and exhibits relatively high light output, though its intrinsic radioactivity, originating from ^{176}Lu beta decay, must be considered in certain applications [4,27]. Despite this, its fast decay and strong luminescence have made it particularly suitable for time-of-flight PET (TOF-PET) systems [5]. Intrinsic luminescence in Ce-doped $(Lu,Y)_2SiO_5$ (LYSO:Ce) single crystals has been investigated using vacuum-ultraviolet (VUV) excitation spectroscopy under synchrotron radiation [28,29]. A previously unreported emission band at ~250 nm was observed, with its thermal behavior characterized between 10 and 120 K, suggesting origins from either the singlet component of self-trapped excitons or self-trapped excitons in the lutetium sublattice. Additionally, Ce^{3+} emission centers with different coordination environments (six- and seven-coordinated) were found to be excited across the VUV range (4.5–8 eV), indicating that the same energy transfer mechanisms from the host lattice to Ce^{3+} are operative regardless of coordination. These results further demonstrate that excitonic processes, involving both intrinsic and bound excitons, dominate the energy transfer to Ce^{3+} luminescence in LYSO.

Advances in crystal growth and processing have further enhanced LYSO performance. Techniques such as the Czochralski method enable the production of high-quality, transparent, and inclusion-free crystals, improving uniformity and scintillation properties [6]. These improvements have solidified LYSO's role as a mainstream scintillator in PET imaging, often paired with photomultiplier tubes (PMTs) or silicon photomultipliers (SiPMs) to optimize timing resolution and system performance [5]. Ongoing research continues to explore LYSO's applications, including its potential in photon-counting detector (PCD) computed tomography (CT) for high-resolution imaging [6].

Recent studies have highlighted strategies to further enhance LYSO:Ce performance through defect engineering and co-doping. Xu et al. [30] demonstrated that annealing at 1200 °C for 10 h effectively reconstructs oxygen vacancy clusters, increases lattice order, raises the photoluminescence quantum yield (PLQY) to 66.01%, improves light output by up to ~52%, and significantly enhances energy resolution. Qiu et al. [31] showed that trace Co^{2+} co-doping (330 ppm) in μ-PD-grown crystals suppresses carrier traps and achieves a

high light yield (∼37,800 ph/MeV), providing an efficient low-level doping strategy. Van der Sar et al. [9] reported that LYSO:Ce is well suited for lower count-rate photon-counting CT applications, while Campbell et al. [32] demonstrated that Ca co-doping modifies Ce valence states (Ce^{3+}→Ce^{4+}) and enables multiple-photon emission, offering a pathway to amplify scintillation signals. Collectively, these studies show that precise control over lattice defects and dopant chemistry can substantially improve the performance of LYSO:Ce in medical imaging and radiation detection.

The development of LYSO scintillators has therefore been marked by significant advancements in crystal growth techniques and a strong focus on optimizing their scintillation properties for medical imaging applications. Their high performance in terms of light output, decay time, and stopping power has established LYSO as a critical component in modern radiation detection technologies.

LYSO scintillators not only exhibit excellent optical and scintillation properties but also possess important mechanical characteristics that affect their performance in detectors [7]. LYSO crystals are valued for their high density, small Molière radius, fast response, and high radiation hardness, making them suitable for applications in high-energy physics and space [8,33].

Mechanical robustness ensures stable optical coupling with PMTs or SiPMs, minimizes crack formation during thermal cycling, and maintains long-term detector reliability. Additionally, rare-earth orthosilicates exhibit moderate but anisotropic thermal expansion. For LSO, Speakman et al. [34] reported strongly anisotropic expansion with average linear coefficients of $\sim$7–8 $\times$ 10^{-6} K^{-1}, with the expansion along the *b*- and *c*-axes being 5–10 times larger than that along the *a*-axis. The thermal expansion of LSO and YSO was found to be similar, with $\Delta L/L_0$ values at 700 °C differing by only about 1–5%. For YSO, Sun et al. [35] and Nowok et al. [36] reported a polycrystalline thermal expansion coefficient in the range $\sim$6.9–8.4 $\times$ 10^{-6} K^{-1}. Such moderate thermal expansion is beneficial for limiting thermally induced dimensional changes under operating conditions.

The application of LYSO in high-energy and nuclear physics has been limited by the availability of high-quality crystals in sufficiently large sizes and by the high cost associated with their high melting point. Nevertheless, large LYSO samples with dimensions of 2.5 $\times$ 2.5 $\times$ 20 cm^3 have been successfully grown and characterized in terms of transmittance, light output, decay kinetics, light-response uniformity, and radiation-induced degradation [3,37]. Compared with BGO ($Bi_4Ge_3O_{12}$) samples of the same size, LSO/LYSO crystals exhibit a much faster decay time and a substantially higher light yield, although their longitudinal light-response uniformity can be affected by variations in Ce concentration and/or Y content. These results confirm the potential of large LSO/LYSO crystals for future large-scale calorimetry applications, while indicating that further optimization and readout studies are still required.

Overall, the combination of high optical performance and adequate mechanical strength makes LYSO a preferred scintillator for high-resolution medical imaging and high-energy physics applications. Despite extensive studies of optical and scintillation properties, the mechanical response of YSO–LYSO–LSO solid solutions remains comparatively less explored.

Recent theoretical and experimental studies have established that the elastic and thermo-mechanical properties of rare-earth orthosilicates are sensitive to modifications of the rare-earth sublattice. First-principles investigations of doped Y_2SiO_5 have shown that partial substitution of Y^{3+} by other rare-earth ions induces systematic, nearly linear changes in elastic moduli, elastic anisotropy, Debye temperature, and related thermodynamic quantities, reflecting the strong coupling between local bonding, mass distribution, and lattice dynamics [38]. Complementary theoretical and experimental studies on sto-

ichiometric X2-RE_2SiO_5 compounds (RE = Y, Tb–Lu) further demonstrated that elastic stiffness, sound velocities, and thermo-mechanical stability vary markedly across the rare-earth series, primarily due to the progressive strengthening of RE–O bonds associated with decreasing ionic radius and increasing atomic mass [39,40]. The mechanical response of YSO, LYSO, and LSO has been characterized by multiple complementary techniques including impulse excitation [39,40], four-point bending on single crystals [41], and nanoindentation [42], yielding a Young's modulus in the moderate range of ∼150–180 GPa across all three compounds. The materials are brittle, with low fracture toughness, which requires careful handling during cutting and polishing of large-format crystals [42]. A detailed quantitative review of the available mechanical data, including hardness, fracture toughness, and elastic anisotropy, is provided in Section 3. These properties are critical for producing large, inclusion-free crystals and for fabricating pixelated arrays used in PET and photon-counting CT systems [6]. Existing studies have largely been restricted to either dilute doped systems or stoichiometric end-member compounds, thereby neglecting the mechanically most relevant regime of continuous solid solutions. In solid solutions such as YSO–LYSO–LSO, the substantial yet chemically compatible contrast between Y^{3+} and Lu^{3+} introduces intrinsic configurational disorder, local strain fields, and mass fluctuations that cannot be captured within simple doping or end-member models, therefore a composition-resolved investigation of elastic properties across the full solid-solution range is essential for establishing reliable structure–property relationships and for enabling predictive mechanical design of YSO–LYSO-based functional materials.

In this work, we conduct a systematic study of YSO–LYSO–LSO solid solutions with varying Lu/Y compositions and cation arrangements using the LCAO DFT hybrid method. We evaluate how both the Lu/Y ratio and the cation distribution affect the structural and elastic properties of LYSO solid solutions.

2. YSO, LYSO, and LSO Structural Properties

YSO exhibits two distinct monoclinic polymorphs. The low-temperature so-called X1-YSO polymorph with the space group $P2_1/c$ (Nr. 14) is characterized by isolated silicon-oxygen tetrahedra and two distinct nine-coordinated and seven-coordinated yttrium sites. This $P2_1/c$ phase undergoes a transformation to the high-temperature phase with the space group Nr. 15 (C2/c) around 1190 °C [43,44]. This YSO polymorph, commonly referred to as X2-YSO, is frequently employed in theoretical and experimental studies [38,45], as it provides a more favorable host environment for luminescent ions. Although metastable at low temperatures, the X2 phase can persist upon cooling after the high-temperature phase transition. Our current research focus is specifically on the YSO and LSO phases with space group No. 15, as the investigation aimed to analyze the behavior of the solid solution with varying ratios of yttrium and lutetium ions. In turn, only the monoclinic X2-type structure with space group No. 15 has been experimentally established for LSO under normal conditions. Described dichotomy in the existence of the X1/X2 phases reflects a systematic dependence on the RE^{3+} ionic radius. Rare earths from La to Gd, with larger ionic radii, crystallize predominantly in the $P2_1/c$ (X1) structure, whereas those from Dy to Lu adopt the C2/c (X2) structure. Y and Tb, situated near the crossover region, may accommodate both polymorphs [40,46]. This structural evolution is consistent with the lanthanide contraction, which increases the cation field strength (CFS $= Z_c/r_c^2$) and generally strengthens RE–O bonding for smaller RE^{3+} cations [40].

It should be noted that in the description of monoclinic-centered lattices, particularly in space group Nr. 15, to which both LSO and LYSO belong, the issue of standardization persists. This is due to the possibility of using either body-centered (I2/a) or face-centered (C2/c) descriptions of the structure [47]. Furthermore, the order of lattice constant vectors

and unit cell angles can also vary, and the cell could be chosen as, e.g., B2/b. Speakman et al. provided a detailed illustration of the structural transformation between the C2/c and I2/a crystal settings for this material system (see Figure 1. in Ref [34]). The transformation between the two crystallographic settings is carried out using a pair of mutually inverse matrices. The transition from the B2/b setting to the I2/a setting is defined by the following transformation matrix:

$$\mathbf{T}_{\mathrm{B2/b}\rightarrow\mathrm{I2/a}} = \begin{bmatrix} 0 & 0 & -1 \\ 0 & 1 & 0 \\ 1 & 0 & -1 \end{bmatrix}. \quad (1)$$

Conversely, the reverse transformation from the I2/a setting back to the B2/b setting is performed using the inverse matrix:

$$\mathbf{T}_{\mathrm{I2/a}\rightarrow\mathrm{B2/b}} = \begin{bmatrix} -1 & 0 & 1 \\ 0 & 1 & 0 \\ -1 & 0 & 0 \end{bmatrix}. \quad (2)$$

Throughout this work, all calculated and experimental structural parameters for YSO–LYSO–LSO compounds are reported consistently in the B2/b setting with the unique (high-symmetry) *b*-axis. The experimental structural parameters are listed in Table 1. Values taken from references that used the I2/a setting (marked with an asterisk in Table 1) were converted to B2/b setting using $\mathbf{T}_{\mathrm{I2/a}\rightarrow\mathrm{B2/b}}$ (Equation (2)) prior to comparison.

Table 1. Experimental lattice constants and angles for Y_2SiO_5 and Lu_2SiO_5 (space group Nr. 15 in B2/b setting).

Compound	a (Å)	b (Å)	c (Å)	$\alpha = \gamma$ (°)	β (°)	Reference
Y_2SiO_5	14.59	6.82	10.52	90	122.25	[48]
	14.41	6.72	10.41	90	122.20	[49]
	14.37	6.71	10.40	90	122.19	[50]
	14.402	6.721	10.41	90	122.201	[51] *
	14.453	6.728	10.42	90	122.36	[52] *
	14.4062(4)	6.72810(2)	10.42072(3)	90	122.1938(2)	[53] *
Y_2SiO_5:Ce	14.458(6)	6.749(3)	10.455(4)	90	122.199(4)	[54]
$Lu_{0.194}Y_{1.806}SiO_5$:Ce	14.380(5)	6.711(2)	10.390(4)	90	122.185(3)	[54]
$Lu_{0.61}Y_{1.39}SiO_5$:Ce	14.342(4)	6.6903(17)	10.361(3)	90	122.198(2)	[54]
$Lu_{0.96}Y_{1.04}SiO_5$:Ce	14.336(5)	6.673(2)	10.335(4)	90	122.212(3)	[54]
$Lu_{1.414}Y_{0.586}SiO_5$:Ce	14.271(5)	6.651(2)	10.284(4)	90	122.198(3)	[54]
$Lu_{1.8}Y_{0.2}SiO_5$	14.2583	6.6425	10.2605	90	122.18	[55]
$Lu_{1.8}Y_{0.2}SiO_5$:Ce	14.245(2)	6.635(1)	10.242(1)	90	122.188(10)	[56]
$Lu_{1.82}Y_{0.176}SiO_5$:Ce	14.263(3)	6.6346(12)	10.2421(18)	90	122.202(2)	[54]
Lu_2SiO_5	14.2774(7)	6.6398(4)	10.2465(6)	90	122.2240(10)	[57]
	14.263(2)	6.643(4)	10.250(3)	90	122.19(1)	[34]
	14.33(2)	6.671(6)	10.32(2)	90	122.30(13)	[58]
	14.263	6.644	10.25	90	122.18	[52] *
	14.254(9)	6.641(7)	10.241(8)	90	122.20(8)	[59]
	14.2638(4)	6.6465(2)	10.2550(2)	90	122.175(1)	[60] *
Lu_2SiO_5:Ce	14.243(4)	6.6334(16)	10.235(3)	90	122.193(2)	[54]

* Data is converted from I2/a setting in the original paper to B2/b setting using the transformations matrix described with Equation (2).

Crystal structures belonging to space group No. 15 can be described not only using the conventional crystallographic unit cell, but also equivalently in terms of a primitive unit cell. In the case of the YSO–LSO system, the conventional unit cell contains a total of 64 atoms, corresponding to 8 structural units of Y_2SiO_5 or Lu_2SiO_5 [61], while the primitive

cell contains 32 atoms and represents the minimal repeating unit of the lattice with the smallest possible volume, with 4 structural units. In the present calculations, the primitive cell was adopted in CRYSTAL calculations in order to reduce the computational costs. A detailed definition of the used primitive cell and its transformation to the conventional crystallographic cell (B2/b setting) using the transformations described in Ref. [62] is provided in the Supplementary Information S2.

The used primitive cell of Y_2SiO_5 and Lu_2SiO_5 with 32 atoms is shown in Figure 1. Eight yttrium atoms are substituted with lutetium in different ways, creating Y/Lu substitution patterns and producing 76 symmetry-independent structures in total. For clarity, representative lowest-energy configurations for each Y/Lu composition are shown in Figure 2. It should also be noted that the eight rare-earth sites in the primitive cell are not equivalent: they form two crystallographically distinct sets, sites 5–8 and 1–4 in Figure 1. Sites 5–8 correspond to sixfold-coordinated Y/Lu environments, commonly denoted in the literature as RE2, whereas sites 1–4 correspond to sevenfold-coordinated environments, commonly denoted as RE1 [54,55,57].

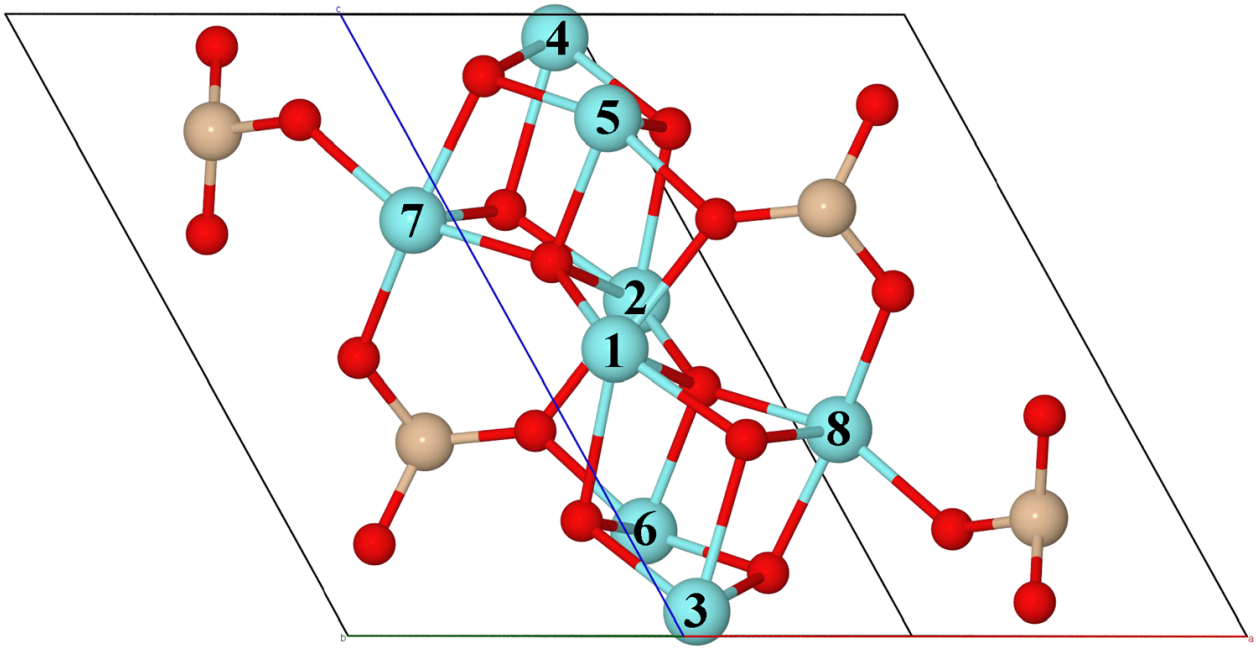


Figure 1. Primitive cell of LYSO (32 atoms, 8 Lu/Y cation sites). Y or Lu atoms are marked with cyan colour, O atoms with red colour, and Si atoms with grey colour. The primitive cell represents the minimal-volume description of the structure used in the present calculations (see Supplementary Information S2 for details on the transformation between primitive and conventional cells). The numbers 1–8 label the eight rare-earth (Y/Lu) sites in the primitive cell, which belong to two crystallographically distinct environments: sites 1–4 correspond to the sevenfold-coordinated environments (denoted RE1 in the literature), and sites 5–8 to the sixfold-coordinated environments (denoted RE2). Eight yttrium atoms are substituted with lutetium in different ways, producing 76 symmetry-independent structures in total.

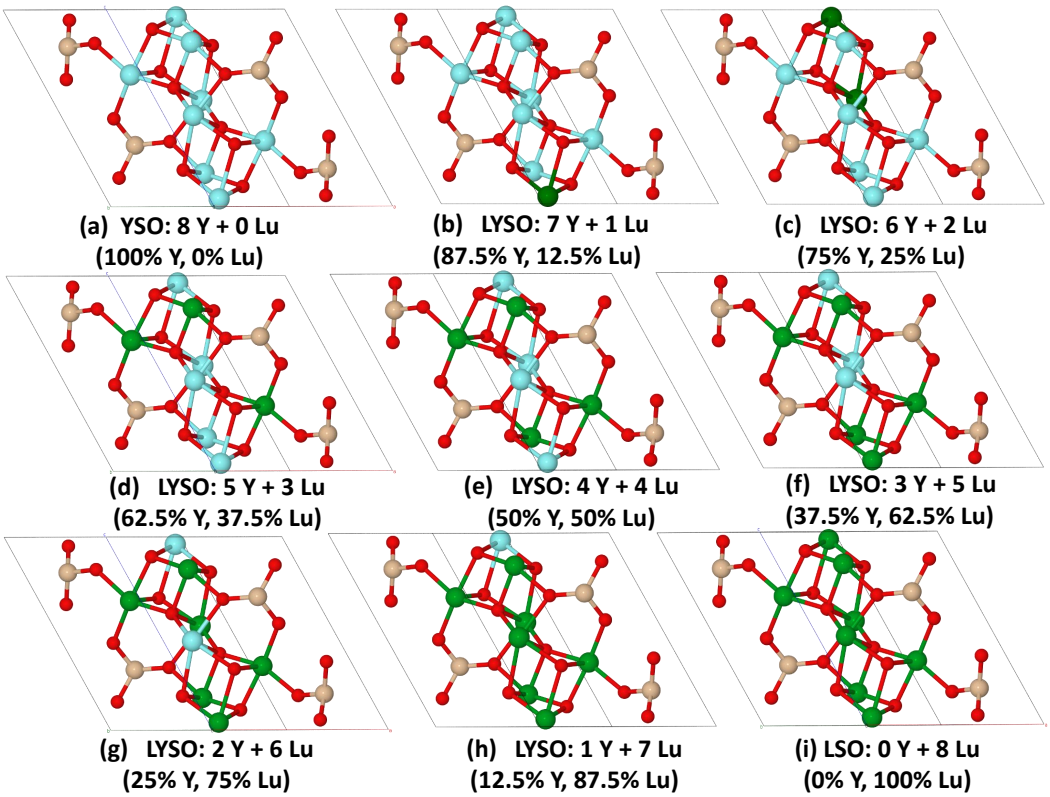


Figure 2. Representative subset of atomic configurations used in this work for the YSO–LYSO–LSO solid-solution series. Y atoms are marked with cyan color, Lu atoms with green color, O atoms with red color, and Si atoms with grey color. The Lu content increases progressively from panels (**a**–**i**). The figure illustrates selected cation substitution patterns within the 32-atom primitive unit cell across the full compositional range, from pure YSO to pure LSO. The configurations shown correspond to the lowest-energy (most stable) arrangements identified for each composition among the total set of 76 symmetry-inequivalent configurations.

3. YSO, LYSO, and LSO Elastic Properties

Since the present study is focused on a systematic *ab initio* description of the elastic properties of LYSO solid solutions, it is instructive to first summarize the existing experimental and theoretical data available for the YSO–LSO compounds and their lightly substituted variants. Previous studies have employed a variety of experimental techniques, including nanoindentation, impulse excitation, bending tests, and heat-treatment analyses, as well as first-principles calculations, to characterize elastic moduli, hardness, fracture behavior, and elastic anisotropy of rare-earth oxyorthosilicates.

This section provides a concise overview of earlier work on the elastic properties of YSO, LYSO, and LSO crystals. Particular attention is paid to the reported values of Young's modulus, shear and bulk moduli, Poisson's ratio, and elastic anisotropy, as well as to the microscopic bonding mechanisms responsible for the observed mechanical behavior.

Nano-indentation experiments applying a controlled load to the crystal surface revealed that LYSO exhibits an average hardness of 11.18 ± 0.50 GPa and a Young's modulus of 155.78 ± 4 GPa. Notably, the modulus remains consistent even as the indentation load increases, underscoring the material's suitability for applications demanding precision [42].

According to the findings reported by Sun et al. using the impulse-excited resonance method, YSO exhibits a Young's modulus of approximately 124 ± 2 GPa and a shear modulus of 47 GPa [35]. The bulk modulus is 108 GPa, and the Poisson's ratio is 0.31. These values suggest that YSO has relatively low stiffness and shear resistance compared with other ceramic materials. Vickers microhardness testing applying loads

up to 50 N demonstrated a hardness of 5.3 ± 0.1 GPa, and the Chevron-notched beam method was used to measure the fracture toughness, which was 1.85 ± 0.17 MPa·$m^{1/2}$. The DFT calculations were also employed to investigate the equilibrium crystal structure and bonding characteristics of YSO using the CASTEP code. The equilibrium crystal structure of YSO was determined by applying Vanderbilt-type ultrasoft pseudopotentials and the generalized gradient approximation for geometry optimization. The analysis revealed that the Si–O bonds within the –SiO_4– tetrahedra exhibit strong covalent character. In contrast, the Y–O bonds are relatively weaker. The primary factor contributing to YSO's low resistance to shear deformation is attributed to the bonding characteristics, particularly the weak Y–O bonds within the –YO_6– and –YO_7– polyhedra. Conversely, the rigid –SiO_4– tetrahedra remain relatively unaffected by mechanical strain, allowing for energy dissipation through mechanisms such as micro-cleavage and crack deflection. A more recent experimental study by Wagner et al. [63] characterized the temperature-dependent elastic response of Eu^{3+}:Y_2SiO_5 single crystals using mechanical spectroscopy, reporting a room-temperature Young's modulus of ∼ 150 GPa and a zero-temperature extrapolated value of $E_0 \approx 158$ GPa, together with a Debye temperature of $\Theta_D \approx 550$ K derived from the temperature dependence of elastic resonances.

The Young's modulus of polycrystalline LSO and YSO has been measured experimentally with the impulse excitation technique to be ∼172–176 GPa and 155 GPa, respectively [40,64], indicating that LSO is slightly stiffer. Bending and tensile tests on Czochralski-grown $Lu_{1.8}Y_{0.2}SiO_5$:Ce single crystals yielded Young's moduli in the range of 129–186 GPa, with an average of ∼180 GPa [41,56]. The monoclinic symmetry of both compounds, combined with the structural contrast between the rigid SiO_4 tetrahedra and the softer rare-earth–oxygen polyhedra (LuO_6/YO_6 and LuO_7/YO_7), gives rise to a pronounced directional dependence of the elastic stiffness constants. Theoretical second-order elastic constants calculated using the CASTEP code were derived from stress–strain relationships obtained using DFT calculations with ultrasoft pseudopotentials and the local density approximation (LDA) [39]. The authors reported single-crystal elastic constants for both Lu_2SiO_5 and Y_2SiO_5; the corresponding effective polycrystalline Young's moduli, obtained from Voigt–Reuss–Hill averaging, are 167 and 150 GPa, respectively. For LSO, the directional Young's modulus exhibits significant anisotropy, ranging from 115 GPa in the least stiff direction to 242 GPa in the stiffest direction; a specific directional analysis of Young's modulus for YSO is not provided in that work. The Poisson's ratio, a parameter that quantifies the ratio between longitudinal and lateral strain in a material under uniaxial stress, is 0.25 for both YSO and LSO compounds [39].

The mechanical interpretation of four-point bending measurements on LYSO single-crystal square cross-section prisms was provided by Davì and Rinaldi [7], who formulated an anisotropic Saint-Venant-type model for monoclinic LYSO specimens and related the measured extensional Young-type modulus to the elastic moduli of the monoclinic crystal. This theoretical treatment was motivated by, and builds on, the earlier experimental work of Scalise et al. [41], where the ultimate tensile strength and Young's modulus of LYSO:Ce single-crystal samples were measured by a four-point bending method along the [010] tensile direction. For LYSO containing 10% yttrium, the Young's modulus was measured using a four-point bending test, yielding an average value of 180 GPa. The crystals displayed brittle elastic behavior and significant anisotropy due to their monoclinic structure, where the elastic response is heavily dependent on the crystallographic orientation. Measurements of ultimate tensile strength (the maximum stress that a material can withstand while being stretched or pulled before breaking) exhibited substantial variability, ranging from 68 MPa to 115 MPa, which was attributed to material defects and differences in annealing. Interestingly, the annealing process appeared to reduce the homogeneity of

both the ultimate tensile strength and Young's modulus, suggesting a detrimental impact of annealing on the overall mechanical performance of the crystals [41].

Density functional theory calculations using the Vienna *Ab initio* Simulation Package (VASP) were performed in Ref. [40] employing the GGA and projector-augmented wave basis set. The elastic properties of rare-earth oxyorthosilicate compounds (RE_2SiO_5) with space group No. 15 crystal structures were investigated, where RE includes Y, Lu, Tb, Dy, Ho, Er, Tm, and Yb. From the 13 independent elastic constants, the Voigt–Reuss–Hill averaging method was used to calculate the bulk modulus, shear modulus, and Young's moduli. Due to the crystal's anisotropy, the minimum and maximum Young's moduli were considered for each compound. The ratio of the maximum to minimum Young's modulus in different crystallographic directions is approximately 2 for all RE_2SiO_5 compounds, indicating significant directional variations in stiffness. Among the maximum Young's modulus values, lutetium oxyorthosilicate exhibits the highest value of 229 GPa, while yttrium oxyorthosilicate shows the lowest value of 183 GPa. Among the minimum values, LSO has the second-highest modulus, slightly lower than Tm_2SiO_5 (127 GPa), while YSO belongs to the compounds with the lowest Young's moduli (113 GPa), slightly exceeding Yb_2SiO_5 (111 GPa) and Tb_2SiO_5 (108 GPa). The differences in elastic stiffness are attributed to the contraction of the RE^{3+} ionic radius, which strengthens the RE–O bonds and enhances material rigidity. Poisson's ratio varies slightly among the materials, with typical values around 0.20–0.25. Additionally, the longitudinal and transverse sound velocities were derived from the elastic moduli, and these were used to calculate properties such as the Debye temperature. Their study demonstrated a clear increase in elastic stiffness with decreasing ionic radius of the RE^{3+} cation and highlighted the key role of relatively soft RE–O polyhedra in controlling the mechanical response, while rigid SiO_4 tetrahedra remain largely unaffected. However, that work focused exclusively on stoichiometric end-member compounds and did not address configurational effects or compositional disorder in YSO–LSO solid solutions, which are central to the present study.

A complementary experimental study by the same group [64] focused specifically on dense polycrystalline Lu_2SiO_5 fabricated by in situ hot pressing/reaction sintering at 1500 °C. The room-temperature Young's modulus, bulk modulus, shear modulus, and Poisson's ratio of Lu_2SiO_5 were reported as $E = 176$ GPa, $B = 113$ GPa, $G = 71$ GPa, and $\nu = 0.24$, respectively, providing an independent and self-consistent set of elastic parameters for the LSO end-member. Vickers microhardness was found to plateau at $\sim 8.9 \pm 0.2$ GPa for indentation loads above 30 N, while the fracture toughness measured by the single-edge notched-beam method was $K_{Ic} = 2.2 \pm 0.1$ MPa·m$^{1/2}$ and the four-point bending strength was $\sigma_b = 218 \pm 7$ MPa. Both fracture toughness and bending strength of LSO are higher than the corresponding values reported for Y_2SiO_5 [35], in line with the expected stiffening upon Y to Lu substitution. The Young's modulus of Lu_2SiO_5 retained $\sim$88% of its room-temperature value at 1377 °C, demonstrating excellent high-temperature elastic stability.

Mirzai et al. employed DFT with the GGA functional, as implemented in the VASP code, to investigate the effects of europium (Eu^{3+}) doping on the mechanical and thermodynamic properties of YSO [38]. The elastic constants were determined using both stress–strain and strain–energy methods. The undoped YSO crystal exhibited a bulk modulus of 105.56 GPa, a shear modulus of 59.66 GPa, and a Young's modulus of 150.61 GPa, with a Poisson's ratio of 0.262, indicating moderate stiffness and mechanical stability. Additionally, the researchers calculated the Debye temperature ($\Theta_D \approx 514$ K for undoped YSO) and a spatial representation of Young's modulus for the material.

Jang et al. investigated the thermal behavior and mechanical characteristics of YSO following isothermal heat treatment at varied temperatures and durations [65]. The as-

sprayed samples displayed a Martens hardness of 4.8 GPa and a Young's modulus of 127 GPa. Both properties exhibited a steady increase, reaching up to 5.8 GPa and 155 GPa, respectively, with prolonged heat treatment times and higher treatment temperatures. This enhancement was attributed to improved crystallization and the formation of monoclinic β-Y_2O_3 phases.

LYSO:Ce single crystals were grown from the melt using the Czochralski technique, with a nominal composition of $Lu_{1.8}Y_{0.2}SiO_5$:Ce [56]. The cerium concentration in the melt was maintained below 1 atomic percent. The results demonstrate that thermal annealing at 300 °C for 10 h influences the mechanical properties of the crystals. The ultimate tensile strength and Young's modulus were found to range from 68–114 MPa and 129–186 GPa, respectively. The crystallographic structure of the samples was investigated through X-ray diffraction and neutron diffraction analyses.

4. Computational Details

4.1. CRYSTAL Calculation

Ab initio calculations were performed with the CRYSTAL23 program [66]. The PW1PW hybrid functional (PW-GGA with 20% Hartree-Fock exchange) and triple-zeta valence-polarized (TZVP) Gaussian-type basis sets [67,68] were employed. The 20% exact exchange fraction follows the parametrization adopted by Oliveira et al. in the reference developing the basis sets [68]. This functional has been shown to yield accurate structural results for ionic solid compounds and good agreement with experimental lattice parameters. Both equilibrium and strained configurations were fully optimized using analytical energy gradients with respect to atomic coordinates and unit-cell parameters. For the elastic constant calculation, two strained configurations were considered for each symmetry-independent strain (four for monoclinic and six for triclinic crystals), with a dimensionless strain amplitude of 0.01. Elastic properties of isotropic polycrystalline aggregates can be computed from the elastic and compliance constants [69,70] via the Voigt–Reuss–Hill averaging scheme, where Voigt and Reuss approximations produce upper and lower bounds of the bulk modulus, respectively.

Solid solutions were mimicked using a 32-atom primitive cell with 8 rare-earth (Y or Lu) atoms. Nine compositions with various lutetium content were studied from 0% to 100% with a step of 12.5%. Overall, 76 symmetry-independent structures were constructed using a group action theory toolkit for studying solid solutions [71,72] as implemented in CRYSTAL23 code. Geometry optimization and elastic constants calculations were performed for every structure. No symmetry constraints were imposed during the structural optimization. As a result, small deviations from the ideal monoclinic symmetry (space group No. 15) were observed in some configurations (the angles α and γ slightly deviate from 90°). These deviations are minor and arise from local structural relaxation. The resulting distortions were found to be negligible and do not affect the calculated elastic properties or the overall compositional trends.

The convergence threshold on energy for the self-consistent-field (SCF) procedure has been set to 10^{-7} for the structural and elastic calculations. Reciprocal space was sampled using a Monkhorst–Pack scheme [73] with a shrinking factor of 4, corresponding to 24–36 *k*-points in the irreducible part of the Brillouin zone, depending on the symmetry of the structure. The calculated 6×6 elastic stiffness tensors (C_{ij}) for the considered compositions with the lowest energies are provided in Supplementary Information (S1).

4.2. Calculation of Spatial Dependence of Elastic Properties

Spatially dependent elastic properties, such as the spatial dependence of Young's modulus, the spatial dependence of linear compressibility, the spatial dependence of the

shear modulus, and the spatial dependence of Poisson's ratio, were calculated using the ELATE online tool for the analysis of elastic tensors [74].

The Voigt–Reuss–Hill approach is a common method for estimating the effective elastic properties of polycrystalline materials [75]. The Voigt and Reuss models, respectively, provide upper and lower bounds for the elastic moduli.

The Voigt (or upper bound) model assumes a scenario where grains are perfectly fitted, preventing mutual deformation, and resulting in a stiffer material response. This model presumes uniform strain ϵ_{kl} across all grains. Conversely, the Reuss (or lower bound) model assumes uniform stress σ_{kl} across grains, while allowing for variable strains. Consequently, the material exhibits maximum compliance under the Reuss model.

To mathematically represent these two scenarios, the Voigt scheme utilizes the components of the stiffness tensor C_{ij} ($\sigma_{ij} = C_{ijkl}\epsilon_{kl}$), while the Reuss scheme employs the components of the inverse stiffness tensor (compliance tensor) S_{ij} ($\epsilon_{ij} = S_{ijkl}\sigma_{kl}$) [76].

The bulk modulus (K) and shear modulus (G) can be calculated as:

$$K_V = \frac{1}{9}(C_{11} + C_{22} + C_{33}) + \frac{2}{9}(C_{12} + C_{13} + C_{23}) \tag{3}$$

and

$$G_V = \frac{1}{15}(C_{11} + C_{22} + C_{33}) - \frac{1}{15}(C_{12} + C_{13} + C_{23}) + \frac{1}{5}(C_{44} + C_{55} + C_{66}) \tag{4}$$

for the Voigt model, and

$$K_R = (S_{11} + S_{22} + S_{33} + 2(S_{12} + S_{13} + S_{23}))^{-1} \tag{5}$$

and

$$G_R = \left(\frac{4(S_{11} + S_{22} + S_{33}) - 4(S_{12} + S_{13} + S_{23}) + 3(S_{44} + S_{55} + S_{66})}{15}\right)^{-1} \tag{6}$$

for the Reuss model.

To obtain a good approximation of polycrystalline sample properties, the arithmetic mean of the Voigt and Reuss limits is used in the Hill scheme:

$$K_H = \frac{K_V + K_R}{2}, \quad G_H = \frac{G_V + G_R}{2} \tag{7}$$

Finally, both Young's modulus (Y) and Poisson's ratio (ν) are calculated using the same formulas across all schemes, with the corresponding values from each approximation placed accordingly:

$$Y = \frac{9KG}{3K + G}, \quad \nu = \frac{3K - 2G}{2(3K + G)} \tag{8}$$

4.3. Debye Temperature

The Debye temperature is a fundamental parameter in solid state physics that characterizes the highest vibrational mode within a solid and marks the boundary between quantum and classical regimes of lattice vibrations. This fundamental property is directly correlated to the material's elastic properties, as it depends on the mean velocity of sound, which is determined by the elastic moduli and density. Higher Debye temperature values signify stronger interatomic bonds and stiffer lattices, increasing elastic moduli and mechanical hardness [77].

The mean elastic wave velocity v_m (also referred to as the effective sonic velocity) can be determined using the longitudinal velocity

$$v_l = \sqrt{\frac{3K + 4G}{3\rho}} \tag{9}$$

and the transverse velocity

$$v_t = \sqrt{\frac{G}{\rho}} \tag{10}$$

refs. [38,78–80]. Then

$$v_m = \left[\frac{1}{3}\left(\frac{2}{v_t^3} + \frac{1}{v_l^3}\right)\right]^{-1/3} = \left[\frac{1}{3}\left(\frac{2}{\left(\frac{G}{\rho}\right)^{3/2}} + \frac{1}{\left(\frac{3K+4G}{3\rho}\right)^{3/2}}\right)\right]^{-1/3}, \tag{11}$$

where K represents the bulk modulus, G is the shear modulus, and ρ denotes the material density.

The Debye temperature Θ_D can be calculated using the mean sound velocity v_m from Equation (11) and the following formula:

$$\Theta_D = \frac{h}{k}\left(\frac{3nN_A}{4\pi}\frac{\rho}{\mu}\right)^{1/3} v_m, \tag{12}$$

where h and k are the Planck and Boltzmann constants, respectively, N_A is Avogadro's constant, μ denotes the molar mass, and n denotes the number of atoms per formula unit [78,80].

5. Results and Discussion

5.1. Structural Properties of YSO–LSO Solid Solutions

Figure 3 shows the mixing energies of YSO and LSO, calculated with respect to pure compound energies as follows:

$$E_{mix} = E_{tot} - x_{Lu} \cdot E_{LSO} - (1 - x_{Lu}) \cdot E_{YSO} \tag{13}$$

where E_{tot} is the total energy of the solid solution, E_{YSO} and E_{LSO} are the total energies of pristine yttrium and lutetium orthosilicates, respectively, and x_{Lu} is the Lu fraction on the rare-earth sublattice, ranging from 0 for YSO to 1 for LSO.

Out of the 76 symmetry-independent optimized configurations, 41 exhibit mixing energies that are zero or negative, indicating an energetic stabilization upon Y/Lu substitution and implying thermodynamic favorability of these configurations.

To estimate the thermodynamic behavior of the system, additional data on the vibrational contribution to the free energy for selected configurations (including pure YSO, LSO, and representative lowest-energy solid solutions) are provided in the Supplementary Information (Excel file S3). The results show that the inclusion of vibrational ($-$TS) contributions at 300 K modifies the relative energies by approximately 10 meV on average, while preserving the energetic ordering of configurations. Therefore, the conclusions based on the total-energy calculations remain valid for larger temperatures.

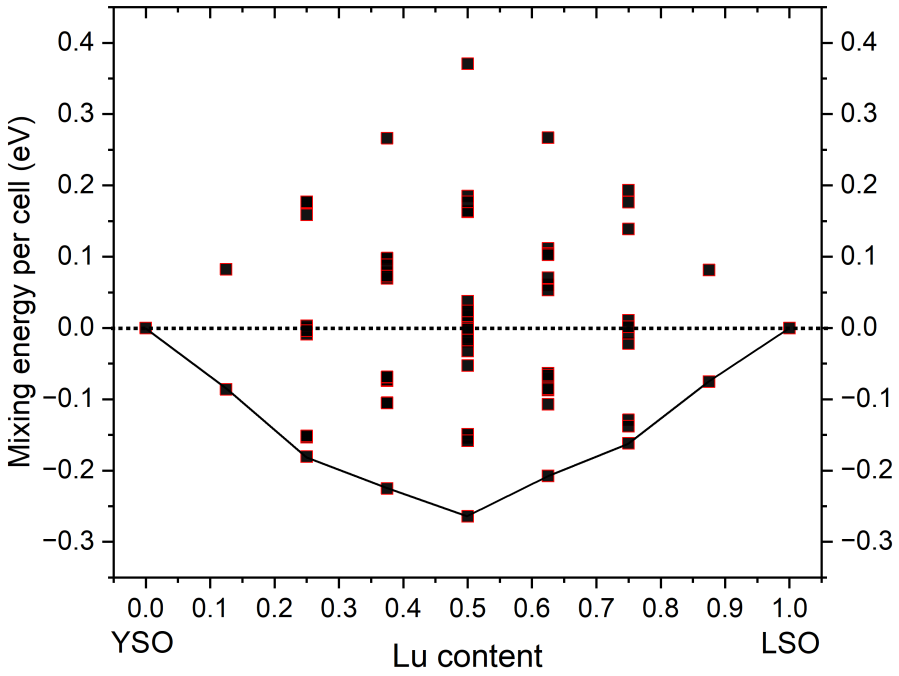


Figure 3. Mixing energies of all 76 YSO–LSO configurations. The dotted line indicates zero energy. A solid black line connects all configurations with the lowest energies. The data refers to the LYSO primitive cell with 32 atoms, with 8 Y/Lu cation positions.

Table 2 summarizes the structural parameters of the lowest-energy configurations as a function of Lu concentration and substitution pattern. Multiplicity M denotes the number of crystallographically equivalent Y/Lu substitution configurations. In other words, it counts how many distinct atomic arrangements are generated by symmetry operations of the parent crystal that have identical total energy and structural parameters. It reflects the configurational degeneracy of a given substitution pattern. Probability P represents the Boltzmann probability of finding a specific substitution configuration at T = 293 K. It is calculated from the relative total energies of all symmetry-independent configurations at the same composition, taking into account their multiplicities.

The mass density of each configuration was calculated using the equilibrium unit-cell volume from Table 2 and the corresponding chemical composition of the conventional monoclinic unit cell in the B2/b setting. The conventional unit cell contains eight formula units ($Z = 8$) of R_2SiO_5 (R = Y, Lu), i.e., 16 rare-earth cations, 8 Si atoms, and 40 O atoms.

In Table 2, the parameter n_{Lu} (ranging from 0 to 8) denotes the number of substituted Lu atoms among eight symmetry-distinct rare-earth sites in the configurational model. Therefore, the total number of Lu and Y atoms in the conventional unit cell is given by

$$N_{Lu} = 2n_{Lu}, \qquad N_Y = 16 - 2n_{Lu}. \tag{14}$$

The mass of the unit cell was computed as

$$m_{cell} = \frac{N_{Lu}M_{Lu} + N_Y M_Y + 8M_{Si} + 40M_O}{N_A}, \tag{15}$$

where M_i are the atomic molar masses and N_A is Avogadro's number.

Finally, the mass density was obtained from

$$\rho = \frac{m_{cell}}{V}, \tag{16}$$

where the equilibrium unit-cell volume V is taken from Table 2 and converted from Å^3 to cm^3. This approach yields an individual density value for each symmetry-independent configuration.

Table 2. Structural data for lowest energy compositions with number of Lu atoms (n_{Lu}), Lu % percentage (x_{Lu}), multiplicity (M), positions of substituted atoms (D, see Figure 1), cell parameters (a, b, c in Å, and α, β, γ in degrees, in B2/b setting), volume (V in Å^3), probability (P) of finding that structure at 293 K, as well as density ρ in g/cm^3. All structures were optimized using a 32-atom primitive cell, and the reported structural parameters correspond to the equivalent conventional B2/b representation. Small deviations of the lattice angles α and γ from 90°, expected for the ideal monoclinic symmetry (space group No. 15), arise due to unconstrained structural relaxation; however, these distortions remain minor and do not affect the overall structural trends.

n_{Lu}	x_{Lu}	M	D	a	b	c	α	β	γ	V	P	ρ
0	0	1	-	14.499	6.710	10.385	90.00	122.22	90.00	854.7	1	4.444
1	0.125	4	3	14.460	6.684	10.355	90.20	122.27	90.10	846.2	0.999	4.826
2	0.25	2	2-4	14.416	6.663	10.329	90.00	122.32	90.00	838.4	0.504	5.212
		4	4-8	14.422	6.658	10.330	89.62	122.31	89.78	838.3	0.321	5.212
		2	1-4	14.422	6.664	10.327	90.00	122.30	90.00	838.9	0.172	5.209
3	0.375	4	5-7-8	14.379	6.639	10.303	90.15	122.35	90.14	830.9	0.974	5.603
4	0.5	1	5-6-7-8	14.344	6.611	10.275	90.00	122.40	90.00	822.8	0.834	6.005
		4	2-6-7-8	14.347	6.619	10.253	90.01	122.32	90.41	822.7	0.043	6.006
		4	1-6-7-8	14.351	6.618	10.251	89.64	122.30	90.18	822.9	0.035	6.005
5	0.625	4	3-5-6-7-8	14.310	6.593	10.226	90.16	122.37	89.73	814.9	0.956	6.414
6	0.75	2	2-3-5-6-7-8	14.282	6.573	10.172	90.00	122.34	90.00	806.7	0.595	6.834
		2	3-4-5-6-7-8	14.283	6.579	10.180	90.32	122.35	89.47	808.1	0.232	6.822
		2	2-4-5-6-7-8	14.286	6.583	10.176	90.00	122.31	90.00	808.8	0.163	6.816
7	0.875	4	1-2-4-5-6-7-8	14.260	6.562	10.127	89.86	122.32	90.26	800.8	0.998	7.241
8	1	1	1-2-3-4-5-6-7-8	14.239	6.547	10.079	90.00	122.33	90.00	793.9	1	7.664

The obtained density values agree well with the reported values equal to 4.5 g/cm^3 for YSO [26,81,82], 7.4 g/cm^3 for LSO [26,81,83,84] and 4.9–6.5 g/cm^3 for different LYSO variations [26]. The unit-cell volume exhibits a pronounced decrease with increasing Lu content, from 854.7 Å^3 for the Lu-free structure to 793.9 Å^3 for the fully substituted composition.

Both dependencies (density ρ and conventional unit-cell volume V as functions of Lu content) are shown in Figure 4. The available experimental density data is also included and shows good agreement with the calculated trend.

The linear trends observable in the figure were obtained using a least-squares linear regression of the form

$$y = kx + d, \tag{17}$$

where x is the Lu content (in at.%) and y corresponds to either the density ρ or the unit cell volume V.

The fitting parameters k (slope) and d (intercept) were determined by minimizing the sum of squared residuals between the calculated data points and the linear model. In practice, this was implemented using a first-order polynomial fit (NumPy `polyfit`).

The quality of the fit was evaluated using the coefficient of determination R^2, defined as

$$R^2 = 1 - \frac{\sum_i \left(y_i - y_i^{\mathrm{fit}}\right)^2}{\sum_i \left(y_i - \bar{y}\right)^2}, \tag{18}$$

where y_i are the calculated values, y_i^{fit} are the fitted values, and $\bar{y}$ is the mean of the dataset.

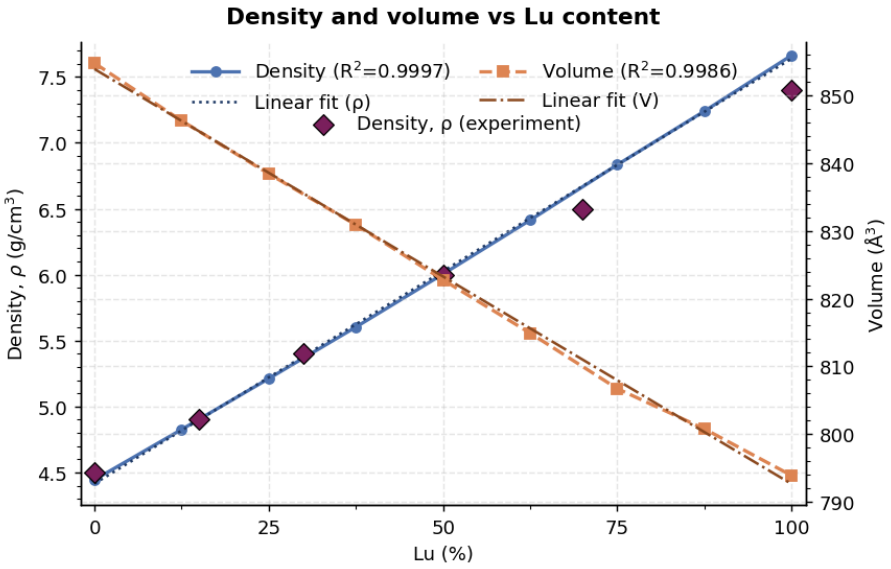


Figure 4. Density and conventional unit-cell volume of YSO-LYSO solid solutions with 64 atoms as a function of Lu content. Solid lines represent calculated values, dashed lines correspond to linear fits, and diamonds indicate available experimental density data [26,81–84]. The nearly linear behavior is further confirmed by the high values of the coefficient of determination with R^2 values close to 1, demonstrating that a simple linear model provides an excellent approximation of the composition dependence of the considered properties.

The obtained high R^2 values ($R^2 = 0.9997$ for the density and $R^2 = 0.9986$ for the unit cell volume) indicate an almost perfectly linear dependence of both density and unit cell volume on the Lu content.

This trend is consistent with Vegard's law, which predicts a linear dependence of a structural parameter on composition,

$$V(x) = (1 - x)\, V_{\mathrm{Y}} + x\, V_{\mathrm{Lu}}, \tag{19}$$

where $x = x_{\mathrm{Lu}}$, and V_{Y} and V_{Lu} denote the unit-cell volumes of the Y-rich and Lu-rich end members, respectively.

A similar Vegard-like behavior is observed for the lattice parameters a, b, and c, which decrease smoothly and monotonically with increasing Lu content, as illustrated in Figure 5. The calculated values agree well with the available experimental data from Table 1: the monotonic decrease of a, b, and c is correctly reproduced, while the monoclinic angle β remains nearly composition-independent and falls within the experimental scatter. The absence of discontinuities or anomalous changes across the entire compositional range indicates that Lu substitution does not induce structural instabilities or symmetry breaking, but instead results in a uniform lattice contraction driven by the smaller ionic radius of Lu^{3+} compared with Y^{3+}, with the high R^2 values (R^2 = 0.9872 for a, R^2 = 0.9875 for b, and R^2 = 0.9793 for c) which confirm an excellent linear description of all considered structural parameters. Despite accurately reproducing the overall trend for LSO, the calculated theoretical values are slightly lower (within about 5%) than those obtained from experimental measurements.

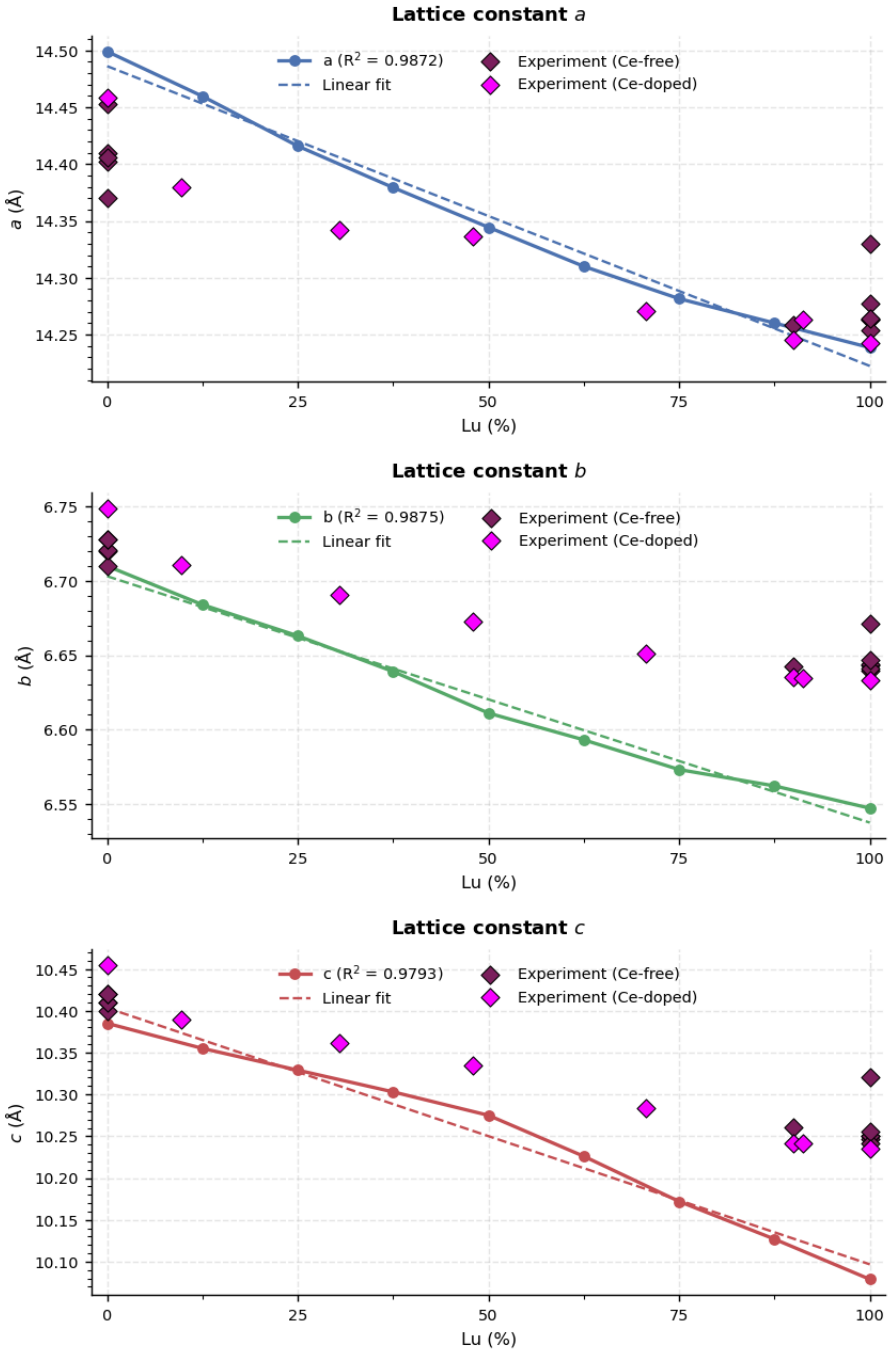


Figure 5. Lattice parameters a, b, and c of Y_2SiO_5–Lu_2SiO_5 solid solutions as a function of Lu content. Solid lines represent calculated values, dashed lines correspond to linear fits, and symbols denote experimental data for Ce-free (dark red diamonds) and Ce-doped (magenta diamonds) samples from Table 1 (see the specific values in the table for a point-by-point comparison with the experimental data). The reported R^2 values (coefficients of determination) quantify the quality of these fits, with values close to 1 indicating an excellent linear correlation.

The lattice angles α, β, and γ remain nearly constant, with deviations below approximately 0.5°. This points to the fact that for YSO–LSO compounds, changes in bond lengths are more important than bond angles that preserve the monoclinic crystal framework.

From a thermodynamic perspective, most compositions are dominated by a single configuration with probability $P \approx 1$ at 293 K, indicating a well-defined ground state. However, for intermediate compositions ($x_{Lu} = 0.25$ and 0.75), several configurations lie

within a narrow energy window, leading to a redistribution of probabilities among multiple substitution patterns.

The preferred substitution patterns evolve systematically with Lu content. At low concentrations, Lu^{3+} ions occupy both seven- and six-coordinated sites, resulting in mixed substitution patterns that minimize local strain. At intermediate compositions, multiple competing configurations with different distributions of Lu over the two crystallographically distinct sublattices become energetically comparable, giving rise to a configurationally sensitive regime. At higher Lu contents ($n_{Lu} > 4$), the lowest-energy configurations increasingly favor occupation of the more compact six-coordinated sites, leading to a more uniform and clustered arrangement of Lu ions within the rare-earth framework (see Figure 2). Despite this clustering tendency, the macroscopic lattice parameters remain well described by Vegard's law, indicating efficient strain accommodation within the crystal lattice.

Table 3 shows the statistical characteristics of Y–O and Lu–O interatomic distances within the considered coordination shells in YSO–LSO solid solutions. The average Y/Lu–O distances decrease nearly monotonically with increasing Lu content, from ∼2.36 Å in YSO to ∼2.27 Å in LSO, reflecting the smaller ionic radius of Lu^{3+} and the resulting lattice contraction.

Table 3. Statistical characteristics (minimum, maximum, average, and median) of the Y/Lu–O atomic distance for YSO–LSO solid solutions.

Statistic	YSO	Lu 12.5%		Lu 25%		Lu 37.5%		Lu 50%		Lu 62.5%		Lu 75%		Lu 87.5%		LSO
		Y	Lu	Y	Lu	Y	Lu	Y	Lu	Y	Lu	Y	Lu	Y	Lu	
MIN	2.208	2.204	2.150	2.204	2.146	2.201	2.142	2.212	2.146	2.201	2.142	2.231	2.134	2.218	2.138	2.130
MAX	2.936	2.890	3.059	2.775	3.012	2.733	2.955	2.542	2.834	2.561	2.904	2.531	2.891	2.511	2.908	2.654
AVER	2.362	2.355	2.333	2.350	2.324	2.346	2.316	2.344	2.305	2.343	2.300	2.347	2.295	2.344	2.294	2.267
MEDI	2.312	2.318	2.225	2.313	2.223	2.322	2.229	2.321	2.232	2.326	2.227	2.324	2.239	2.320	2.233	2.233

At intermediate compositions, Y–O bonds remain systematically longer than Lu–O bonds, indicating the persistence of distinct local coordination environments rather than a fully averaged rare-earth sublattice. The spread between minimum and maximum bond lengths decreases toward Lu-rich compositions, pointing to a more compact and less deformable Lu–O polyhedral network.

A comparison of our results for Y–O bond lengths in YSO with the data of Ching et al. [85] shows good agreement. Using the orthogonalized linear combination of atomic orbitals (OLCAO) method, Ching et al. quantified the strength of individual Y–O contacts through the Mulliken bond order $\rho_{\alpha\beta}$, calculated from the eigenvector coefficients and the inter-orbital overlap matrix in a minimal-basis representation (Equation (2) and Table III of Ref. [85]). In their structural model, the seven-coordinated Y1 site exhibits Y–O distances ranging from 2.199 to 2.604 Å, whereas the six-coordinated Y2 site has a narrower range of 2.203–2.287 Å. The longest Y1–O2 contact, 2.604 Å, has the smallest Mulliken bond order, $\rho_{Y1-O2} = 0.085$, substantially lower than most other Y–O bond orders ($\rho_{Y-O} \approx 0.13$–0.19). This long and weak contact corresponds to the outermost oxygen in the sevenfold-coordinated Y1 polyhedron and may therefore be regarded as a weak peripheral contact rather than as one of the dominant Y–O bonds. Excluding this bond, the remaining Y–O distances reported by Ching et al. lie within approximately 2.20–2.37 Å, in close agreement with the Y–O bond-length range obtained in the present work (Table 3).

Minor non-monotonic variations of the extreme values at intermediate Lu contents originate from different Y/Lu substitution patterns and local strain accommodation. The systematic offset between the average and median Y/Lu–O distances (the mean lying above the median) reflects a right-skewed bond-length distribution: the seven-coordinated RE1 site contributes one long, weak peripheral RE–O contact (up to ∼2.9 Å) that shifts the mean upward relative to the median. This asymmetry is most pronounced for the

Y–O distances, consistent with the longer and softer Y–O bonds, and decreases toward the Lu-rich compositions, where the more compact six-coordinated environment narrows the distribution. Overall, the progressive shortening of Y/Lu–O bonds provides a microscopic basis for the increase in elastic stiffness observed with increasing Lu concentration.

5.2. Mechanical Properties of YSO–LSO Solid Solutions

Table 4 summarizes the elastic properties (bulk modulus K, shear modulus G, Young's modulus Y, and Poisson's ratio ν) obtained from CRYSTAL23 [66] calculations using the Hill averaging scheme. The relative total energies of different Y/Lu substitution patterns are also listed. With increasing Lu content, the bulk modulus (K_V, K_R, and K_H) generally increases, indicating enhanced lattice stiffness. However, the increase in bulk modulus is non-linear. The bulk modulus displays an increase from approximately 92 GPa for pure YSO to about 115 GPa for pure LSO. The shear modulus (G) and Young's modulus (Y) also generally increase with the increase in Lu% content, suggesting that the material becomes increasingly resistant to shape changes under applied force. In turn, Poisson's ratio (ν) exhibits slight fluctuations as the composition changes.

Table 4. Mechanical properties of YSO–LSO solid solutions. Bulk modulus K_V, K_R, and K_H calculated using Voigt, Reuss, and Hill schemes, and shear modulus G_H, Young's modulus Y_H, and Poisson's ratio ν_H calculated using Hill scheme, as implemented in CRYSTAL code [66]. Difference in total energy is also listed.

x_{Lu}	ΔE, meV	K_V, GPa	K_R, GPa	K_H, GPa	G_H, GPa	Y_H, GPa	ν_H
0	-	95.53	87.84	91.68	61.71	151.21	0.225
0.125	-	105.16	99.87	102.51	64.65	160.27	0.239
0.25	-	110.59	106.79	108.69	66.83	166.39	0.245
	27.1	109.17	104.13	106.65	66.22	164.60	0.243
	28.9	106.45	100.85	103.65	65.54	162.39	0.239
0.375	-	108.45	102.72	105.58	66.64	165.17	0.239
0.5	-	108.24	101.80	105.02	67.44	166.65	0.236
	110.1	108.26	102.70	105.48	68.21	168.35	0.234
	115.4	107.98	101.47	104.72	67.63	166.95	0.234
0.625	-	110.60	104.19	107.39	68.79	170.07	0.236
0.75	-	111.49	106.15	108.82	70.88	174.71	0.232
	23.8	112.92	105.34	109.13	69.86	172.73	0.236
	32.7	112.93	105.81	109.37	69.72	172.50	0.237
0.875	-	115.07	108.29	111.68	71.56	176.89	0.236
1	-	118.01	111.01	114.51	72.75	180.11	0.238

Table 5 summarizes the elastic properties of the YSO–LSO solid solutions (bulk modulus K, Young's modulus Y, shear modulus G, and Poisson's ratio ν) calculated using Voigt, Reuss, and Hill approximations, averaging schemes derived from the initial elastic constant tensor obtained in CRYSTAL calculations, as implemented in the ELATE online tool [74]. These trends are also illustrated in Figure 6. Because Young's modulus is the most consistently reported property, the detailed quantitative comparison focuses mainly on Y.

The elastic properties of YSO–LSO solid solutions exhibit clear systematic trends with increasing Lu content x_{Lu}. The bulk modulus K, Young's modulus Y, and shear modulus G all show an overall increase as Lu progressively substitutes Y, indicating a gradual stiffening of the lattice from YSO toward LSO for each Voigt, Reuss, and Hill approximation.

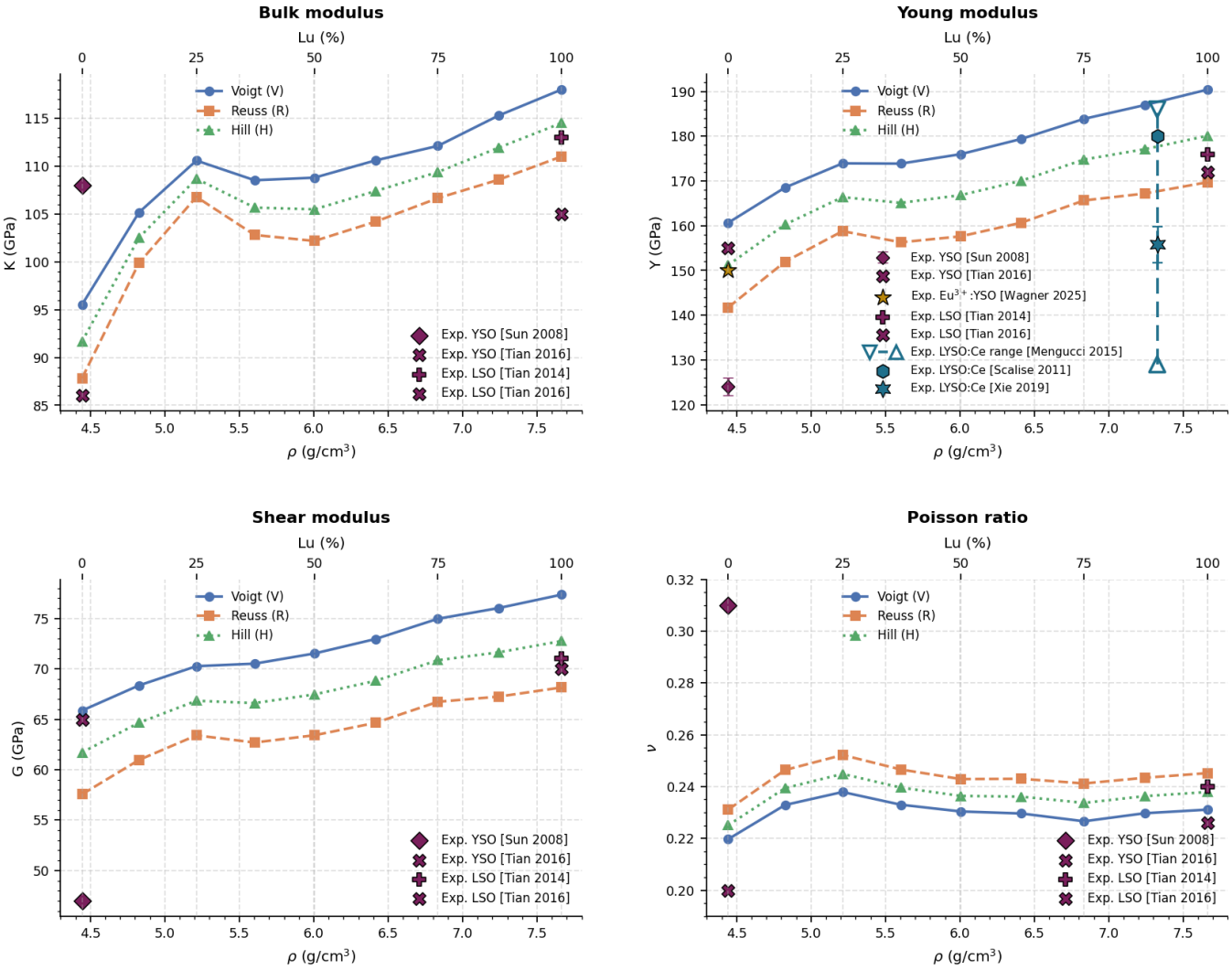


Figure 6. Elastic properties of YSO–LYSO–LSO solid solutions as a function of density (bottom axis) and Lu content (top axis): bulk modulus K, Young's modulus Y, shear modulus G, and Poisson's ratio ν calculated with the ELATE online tool using Voigt, Reuss, and Hill approximations [74]. Experimental data, where available, are shown for the corresponding moduli: dark magenta symbols correspond to undoped (Ce-free) YSO and LSO measurements (Sun 2008 [35], Tian 2014 [64], Tian 2016 [40]); dark teal symbols correspond to Ce-doped LYSO single crystals (Scalise 2011 [41], Mengucci 2015 [56], Xie 2019 [42]); the dark gold star indicates the recent room-temperature Young's modulus of Eu^{3+}:YSO (Wagner 2025 [63]).

Minor non-monotonic variations are observed at intermediate LYSO compositions (notably around $x_{Lu} = 0.25$). Non-monotonicity observed for the elastic moduli and Poisson's ratio at intermediate Lu concentrations, with the local maximum at 25% Lu content, reflects the configurational nature of the Y/Lu solid solution. The substitution of Y by the smaller Lu cation generally shortens the Y/Lu–O bonds and increases the stiffness of the rare-earth–oxygen polyhedral framework. However, at intermediate compositions, the elastic response depends not only on the total Lu content but also on the occupation of the two crystallographically distinct rare-earth sublattices. In the present structural model, two crystallographically inequivalent Y/Lu positions are present: sites 1–4 correspond to the seven-coordinated Y/Lu positions, whereas sites 5–8 correspond to the six-coordinated Y/Lu positions. At low Lu concentrations, substitution occurs at both seven-coordinated and six-coordinated sites, as evidenced by the mixed substitution patterns in Table 2. With increasing Lu content, the lowest-energy configurations increasingly favor six-coordinated

sites 5, 6, 7, and 8. This crossover from mixed to preferential six-coordinated site occupation introduces a transitional compositional regime in which the elastic response reflects competing contributions from Lu at both sublattices, locally suppressing the monotonic stiffening trend.

Table 5. Elastic properties of YSO–LSO solid solutions obtained using the Voigt, Reuss, and Hill approximations for configurations with the smallest energy: bulk modulus K, Young's modulus Y, shear modulus G, and Poisson's ratio ν calculated with ELATE online tool [74].

x_{Lu}	K (GPa)			Y (GPa)			G (GPa)			ν		
	Voigt	Reuss	Hill	Voigt	Reuss	Hill	Voigt	Reuss	Hill	Voigt	Reuss	Hill
0.000	95.53	87.84	91.68	160.66	141.73	151.21	65.86	57.56	61.71	0.2197	0.2311	0.2251
0.125	105.16	99.87	102.51	168.54	151.96	160.27	68.35	60.96	64.65	0.2329	0.2464	0.2394
0.250	110.59	106.79	108.69	173.94	158.79	166.39	70.26	63.40	66.83	0.2379	0.2522	0.2449
0.375	108.53	102.81	105.67	173.88	156.29	165.11	70.51	62.69	66.60	0.2330	0.2466	0.2396
0.500	108.80	102.18	105.49	175.99	157.62	166.83	71.52	63.41	67.46	0.2304	0.2429	0.2364
0.625	110.60	104.19	107.39	179.41	160.68	170.07	72.95	64.64	68.80	0.2296	0.2430	0.2361
0.750	112.12	106.66	109.39	183.89	165.65	174.80	74.96	66.73	70.85	0.2266	0.2412	0.2337
0.875	115.29	108.58	111.93	186.96	167.19	177.10	76.02	67.24	71.63	0.2297	0.2434	0.2363
1.000	118.01	111.01	114.51	190.43	169.73	180.11	77.35	68.15	72.75	0.2311	0.2452	0.2379

5.3. Directional Elastic Properties of YSO–LSO Solid Solutions

Table 6 presents the directional elastic properties of YSO–LSO solid solutions as a function of Lu concentration x_{Lu}, including the minimum and maximum values of Young's modulus Y, linear compressibility β, shear modulus G, and Poisson's ratio ν, together with the corresponding anisotropy factors obtained in the ELATE online tool [74]. Additional visualization of spatial elastic properties is provided in the Supplementary Information (S1).

Table 6. Directional elastic properties of YSO–LSO solid solutions as a function of Lu concentration x_{Lu}: minimum and maximum values of Young's modulus Y, linear compressibility β, shear modulus G, and Poisson's ratio ν, together with the corresponding anisotropy factors calculated with ELATE online tool [74].

x_{Lu}	Y (GPa)			β (TPa^{-1})			G (GPa)			ν	
	Min	Max	Anisotr.	Min	Max	Anisotr.	Min	Max	Anisotr.	Min	Max
0.000	102.70	233.31	2.272	1.4524	5.5415	3.8154	37.31	89.81	2.407	−0.1285	0.5398
0.125	112.81	240.15	2.129	1.6168	4.4973	2.7815	40.48	92.72	2.291	−0.0615	0.5282
0.250	120.58	240.86	1.998	1.7852	4.0227	2.2533	42.51	94.21	2.217	−0.0263	0.5225
0.375	108.91	242.53	2.227	1.5477	4.5778	2.9579	40.82	96.35	2.360	−0.0618	0.5540
0.500	113.18	245.38	2.168	1.3931	4.4572	3.1996	41.18	98.36	2.388	−0.0789	0.5441
0.625	111.29	249.18	2.239	1.4321	4.4068	3.0771	41.63	99.84	2.398	−0.0724	0.5596
0.750	119.19	255.30	2.142	1.5842	4.1442	2.6159	42.78	102.33	2.392	−0.0516	0.5343
0.875	113.53	260.62	2.296	1.4070	4.3199	3.0702	42.76	104.08	2.434	−0.0614	0.5591
1.000	119.90	262.87	2.192	1.3380	4.0515	3.0280	42.73	105.08	2.459	−0.0678	0.5626

The results reveal pronounced elastic anisotropy across the entire compositional range. For all compositions, the ratio between the maximum and minimum values of Young's modulus reaches ∼2, indicating a strong directional dependence of the stiffness. While the minimum values of Y increase moderately with Lu content, the maximum values exhibit a clearer monotonic increase from YSO to LSO, reflecting the overall stiffening of the lattice upon substitution of Y by Lu.

A similar anisotropic behavior is observed for the shear modulus G, with anisotropy factors remaining in the range of approximately 2.2–2.5. Both the minimum and maximum shear moduli increase with increasing x_{Lu}, consistent with the trends obtained from the Hill-averaged elastic constants. In contrast, the linear compressibility β shows the opposite trend: its minimum and maximum values generally decrease toward the LSO compound, indicating reduced compressibility and enhanced resistance to volume deformation with increasing Lu content.

Poisson's ratio exhibits a relatively narrow variation in its maximum values, remaining close to $\nu \approx 0.53$–0.56 for all compositions. Notably, the minimum values of Poisson's ratio ν are negative for all compositions x_{Lu}, which indicates the presence of direction-dependent auxetic behavior in the YSO–LSO solid-solution series. This effect does not imply that the materials are globally auxetic; rather, it reflects a highly anisotropic elastic response in which specific crystallographic directions or deformation modes exhibit lateral expansion under uniaxial loading. Such local auxeticity is typically associated with the underlying crystal topology and the anisotropic connectivity of polyhedral units in low-symmetry lattices. In the YSO–LSO system, the coexistence of rigid SiO_4 tetrahedra and more deformable rare-earth–oxygen polyhedra may be associated with nontrivial deformation mechanisms, including polyhedral rotations and hinge-like motions, which enable negative transverse strain in selected directions. The persistence of negative ν_{min} across the entire compositional range suggests that these mechanisms are intrinsic to the crystal framework and are not suppressed by Lu/Y substitution.

A comparison between our calculated elastic properties presented in this section and the literature data summarized in Section 3 demonstrates overall good qualitative and quantitative agreement, particularly when the differences between single-crystal, polycrystalline, and coating samples, as well as between direct (resonance, bending, tensile) and indirect (nanoindentation) techniques, are taken into account.

For YSO, the Hill-averaged Young's modulus obtained in this work ($Y_H \approx 150$ GPa) lies within the experimental scatter reported in the literature. Sun et al. [35] measured $Y = 124 \pm 2$ GPa on dense polycrystalline YSO using the impulse-excited resonance method, while Tian et al. [40] reported $Y \approx 155$ GPa on YSO polycrystals obtained by the same technique. Plasma-sprayed YSO coatings studied by Jang et al. [65] exhibited a lower as-sprayed Young's modulus of ~127 GPa, increasing up to ~155 GPa after isothermal heat treatment due to improved crystallinity and the formation of the monoclinic β-Y_2O_3 phase.

Recent mechanical-spectroscopy measurements on Eu^{3+}:YSO single crystals [63] yielded a room-temperature Young's modulus of ~150 GPa and a zero-temperature extrapolated value of $E_0 \approx 158$ GPa, together with a pronounced mode-dependent elastic response. The latter is consistent with the picture established by Sun et al. [35] and Tian et al. [40], in which the relatively weak RE–O bonds govern shear deformation and acoustic dissipation, while the rigid SiO_4 tetrahedra remain largely unaffected. Our value of $Y_H \approx 151$ GPa is also consistent with previous DFT results for stoichiometric YSO ($Y \approx 150$–152 GPa) [38–40].

The calculated shear modulus for YSO ($G_H \approx 62$ GPa) is noticeably higher than the resonance-based experimental estimate of ~47 GPa [35]. This discrepancy is consistent with the strong directional dependence of the shear stiffness, with directional shear moduli ranging from ~37 to ~90 GPa in the present calculations (Table 6), and reflects the difference between an orientation-averaged Hill estimate for an idealized polycrystal and a measurement performed on a real sample with finite texture and porosity. The agreement with the theoretical values obtained by Tian et al. ($G_R = 59$ GPa, $G_V = 62$ GPa, $G_H = 60.5$ GPa) [40] is, by contrast, excellent.

For LSO, our Hill-averaged shear modulus ($G_H \approx 73$ GPa) agrees closely with the experimentally derived values of 71 GPa from Tian et al. [64] and ~70 GPa from the X2-RE_2SiO_5 series [40], providing further validation across the LSO end-member.

The calculated bulk modulus for YSO ($K_H \approx 92$ GPa) lies between the experimental value of ~86 GPa reported by Tian et al. from impulse excitation [40] and the value of ~108 GPa derived from the elastic constants measured by Sun et al. [35], and is consistent with previously reported DFT values of 100–106 GPa [38,40]. This spread is in line with the typical variation among different DFT methodologies and the well-known tendency of GGA-type functionals to overestimate the bulk modulus relative to experiment slightly.

For LSO, our Hill-averaged value ($K_H \approx 114.5$ GPa) agrees closely with the experimentally derived value of $B = 113$ GPa reported by Tian et al. [64] and with the VASP/GGA value of $B_H = 114.5$ GPa from [40], while the impulse-excitation estimate of $B = 105$ GPa from the X2-RE_2SiO_5 series [40] is somewhat lower.

The calculated Young's modulus for LSO and Lu-rich LYSO compositions ($Y_H \approx 175$–180 GPa) is in good agreement with the available experimental data for polycrystalline and single-crystal Lu-containing oxyorthosilicates. In particular, Tian et al. [64] reported $E = 176$ GPa, $B = 113$ GPa, $G = 71$ GPa, and $\nu = 0.24$ for dense polycrystalline Lu_2SiO_5 fabricated by *in situ* hot pressing/reaction sintering at 1500 °C, while a subsequent study by the same group on the X2-RE_2SiO_5 series (RE = Tb, Dy, Ho, Er, Tm, Yb, Lu, Y) yielded $E \approx 172$ GPa for Lu_2SiO_5 prepared by two-step reactive sintering followed by hot pressing at 1600 °C [40]. Both independent impulse-excitation measurements lie within a few GPa of our calculated Hill-averaged value of ~180 GPa. Our prediction also matches the average value of ~180 GPa reported by Scalise et al. [41] from four-point bending tests on Czochralski-grown $Lu_{1.8}Y_{0.2}SiO_5$:Ce single crystals (10% yttrium), as well as the range of 129–186 GPa reported on the same set of samples by Mengucci et al. [56], where the lowest values were correlated with the presence of nanoscale coherent precipitates induced by annealing at 300 °C.

The mean nanoindentation value of 155.78 ± 4 GPa reported by Xie et al. [42] for LYSO is somewhat lower than our prediction; this is consistent with the known tendency of nanoindentation on anisotropic monoclinic substrates to probe a depth- and orientation-averaged response that systematically underestimates the maximum directional Young's modulus. Earlier first-principles work [40] reported even higher maximum directional values, exceeding ~229 GPa for LSO, in line with the strong anisotropy ($Y_{max}/Y_{min} > 2$) found in the present study (Table 6).

Finally, the Poisson's ratio obtained in our calculations ($\nu \approx 0.23$–0.25) falls within the range reported in the literature for YSO, LYSO, and LSO. Experimental values span a broader interval, from $\nu \approx 0.20$–0.23 reported by Tian et al. [40] for the X2-RE_2SiO_5 polycrystalline series and $\nu = 0.24$ obtained by the same group for LSO produced by *in situ* hot pressing/reaction sintering [64], to $\nu \approx 0.31$ reported by Sun et al. [35] from resonance measurements on YSO, while previous DFT studies report $\nu \approx 0.25$ [39,40]. The remaining discrepancies between calculated and measured values can be attributed to a combination of elastic anisotropy, differences in averaging schemes, sample-dependent porosity and texture, and the influence of defects, dopants, and thermal history in the experimental samples.

5.4. Sound Velocities and Debye Temperature

Table 7 summarizes the transverse (v_t), longitudinal (v_l), and mean (v_m) sound velocities together with the corresponding Debye temperatures Θ_D for the lowest-energy YSO–LSO configurations. To calculate values, we used Equations (11) and (12), with the Hill-averaged bulk and shear moduli K_H and G (Table 4), and the density ρ computed from the equilibrium unit-cell volume (Table 2). The Debye temperature exhibits a clear and

systematic decrease with increasing Lu content, dropping from approximately 518 K for YSO to about 439 K for LSO.

Table 7. Sound velocities and Debye temperature for the lowest-energy configurations from Table 2, calculated from the density ρ (via equilibrium volume V) and elastic moduli K_H and G (Table 4) using Equations (11) and (12).

x_{Lu}	n_{Lu}	ΔE (meV)	D	V (Å^3)	ρ	K_H (GPa)	G (GPa)	v_t	v_l	v_m	Θ_D
0.000	0	–	–	854.7	4.444	91.68	61.71	3727	6257	4125	518
0.125	1	–	3	846.2	4.826	102.51	64.65	3660	6253	4058	511
0.250	2	–	2–4	838.4	5.212	108.69	66.83	3581	6161	3973	502
0.250	2	27.10	4–8	838.3	5.212	106.65	66.22	3564	6116	3954	499
0.250	2	28.90	1–4	838.9	5.209	103.65	65.54	3547	6056	3933	497
0.375	3	–	5–7–8	830.9	5.603	105.58	66.64	3449	5891	3824	484
0.500	4	–	5–6–7–8	822.8	6.005	105.02	67.44	3351	5697	3714	472
0.500	4	110.10	2–6–7–8	822.7	6.006	105.48	68.21	3370	5719	3734	475
0.500	4	115.40	1–6–7–8	822.9	6.005	104.72	67.63	3356	5697	3719	473
0.625	5	–	3–5–6–7–8	814.9	6.414	107.39	68.79	3275	5572	3630	463
0.750	6	–	2–3–5–6–7–8	806.7	6.834	108.82	70.88	3221	5455	3568	456
0.750	6	23.76	3–4–5–6–7–8	808.1	6.822	109.13	69.86	3200	5445	3547	454
0.750	6	32.72	2–4–5–6–7–8	808.8	6.816	109.37	69.72	3198	5448	3545	453
0.875	7	–	1–2–4–5–6–7–8	800.8	7.241	111.68	71.56	3144	5348	3484	447
1.000	8	–	1–2–3–4–5–6–7–8	793.9	7.664	114.51	72.75	3081	5253	3416	439

This trend reflects the combined influence of two competing factors: the gradual increase in elastic stiffness (bulk and shear moduli) and the pronounced increase in mass density resulting from the substitution of Y by the heavier Lu cation. Although both K_H and G increase with Lu concentration, the accompanying rise in density dominates the acoustic response, leading to a reduction in all sound velocities and, consequently, in Θ_D.

For fixed compositions with multiple symmetry-independent configurations, the variations in Θ_D are relatively small (typically within 5–10 K), indicating that the Debye temperature is only weakly sensitive to the specific Lu/Y substitution pattern. Instead, it is primarily governed by the average composition and associated macroscopic quantities, such as density and elastic moduli. This observation is consistent with the configurational averaging inherent in the Debye model.

The longitudinal sound velocity v_l decreases monotonically from about 6250 m s^{-1} in YSO to approximately 5250 m s^{-1} in LSO, while the transverse velocity v_t shows a similar reduction from roughly 3730 m s^{-1} to about 3080 m s^{-1}. As a result, the mean sound velocity v_m, which directly enters the Debye temperature expression, decreases by nearly 17% across the solid-solution series, in close correspondence with the observed reduction of Θ_D.

Tian et al. reported calculated elastic moduli, sound velocities, and Debye temperatures for the end-member compositions [39]. For YSO, Tian et al. reported a Debye temperature of $\Theta_D = 507$ K, which is in good agreement with our value of $\Theta_D \approx 518$ K. Similarly, for LSO, Tian et al. obtained $\Theta_D \approx 423$ K, which closely matches our calculated value of $\Theta_D \approx 439$ K for LSO.

A comparison of sound velocities reveals a consistent trend. According to Table 3 in Tian et al. [39], the mean sound velocity for LSO is lower than that for YSO, reflecting the effect of the higher atomic mass of Lu and the increased heterogeneity of chemical bonding. In our manuscript, the absolute values of the longitudinal v_l, transverse v_t, and mean v_m sound velocities are close to those reported by Tian et al., namely $v_t = 3002$ m/s, $v_l = 5214$ m/s, and $v_m = 3334$ m/s for LSO, and $v_t = 3580$ m/s, $v_l = 6196$ m/s, and $v_m = 3975$ m/s for YSO. The differences do not exceed the typical level expected from the

use of different DFT methodologies, namely plane-wave CASTEP calculations versus the LCAO-DFT approach adopted in the present work.

Mirzai et al. also evaluated [38] Debye temperature Θ_D for YSO using the elastic-constant-based approach within the Debye–Anderson model, where the elastic moduli were obtained from plane-wave density functional theory calculations. In that work, longitudinal and transverse sound velocities were derived from the Voigt–Reuss–Hill averaged bulk and shear moduli and the crystal density, and subsequently used to determine Θ_D. The Debye temperature of YSO was found to be $\Theta_D \approx 514$ K, in good agreement with our theoretical estimates. In addition, a recent experimental study reported a Debye temperature of approximately $\Theta_D \approx 550$ K for Eu^{3+}:YSO single crystals, derived from the temperature dependence of elastic resonances [63].

Overall, the monotonic evolution of the Debye temperature confirms a progressive softening of lattice vibrational frequencies with increasing Lu content, despite the simultaneous increase in elastic moduli. This behavior is characteristic of solid solutions in which mass effects outweigh stiffness enhancement.

6. Conclusions

We performed systematic *ab initio* calculations of Y_2SiO_5-Lu_2SiO_5 solid solutions across the full compositional range. By explicitly constructing 76 symmetry-independent Y/Lu substitution patterns within a 32-atom primitive cell, both configurational and compositional effects were systematically addressed.

Out of the 76 symmetry-independent configurations, 41 exhibit zero or negative mixing energies, demonstrating the thermodynamic compatibility of Y^{3+} and Lu^{3+} on the rare-earth sublattice across the entire YSO–LSO range. The preferred substitution patterns evolve systematically with composition: at low Lu content, Lu^{3+} ions populate both seven-coordinated (RE1) and six-coordinated (RE2) sites in mixed patterns that minimize local strain, whereas at higher Lu concentrations ($n_{Lu} > 4$) the lowest-energy configurations increasingly favor occupation of the more compact six-coordinated RE2 sites, leading to a more uniform and slightly clustered Lu arrangement within the rare-earth framework.

The calculated lattice parameters and unit-cell volumes exhibit a smooth and nearly linear compositional dependence consistent with Vegard's law, indicating uniform lattice contraction driven by the smaller ionic radius of Lu^{3+} compared with Y^{3+}. This practically important result shows that lattice parameters of LYSO solid solutions can be reliably estimated by linear interpolation, without pronounced structural anomalies. The Y/Lu–O bond-length analysis reveals that Y–O bonds remain systematically longer than Lu–O bonds even at intermediate compositions, indicating that the two crystallographically distinct rare-earth environments preserve their local identity rather than forming a fully averaged sublattice. The progressive shortening of Y/Lu–O bonds with increasing Lu content provides a microscopic basis for the macroscopic stiffening observed in the elastic response.

Hill-averaged bulk, shear, and Young's moduli increase overall with increasing Lu content, reflecting progressive lattice stiffening, while Poisson's ratio remains nearly composition-independent. A non-monotonic local maximum of the elastic moduli is observed near $x_{Lu} = 0.25$, originating from the crossover between mixed and preferential six-coordinated site occupation in the lowest-energy configurations; this configurational sensitivity cannot be captured by end-member or dilute-doping models and constitutes one of the principal findings of the present work. Despite this smooth macroscopic behavior, pronounced elastic anisotropy is preserved across the entire solid-solution series, with directional Young's and shear moduli differing by more than a factor of two. Notably, negative minimum values of Poisson's ratio are found for all compositions, revealing

intrinsic direction-dependent auxetic behavior associated with the low-symmetry monoclinic framework and with the coexistence of rigid SiO_4 tetrahedra and more deformable RE–O polyhedra.

The mean sound velocity decreases by nearly 17% from YSO to LSO, and the Debye temperature systematically decreases from $\Theta_D \approx 518$ K at the YSO end to $\Theta_D \approx 439$ K at the LSO end. This evolution reflects the dominant effect of increasing mass density, which outweighs the concurrent stiffening of the lattice. The Debye temperature is found to be only weakly sensitive (∼5–10 K) to the specific Lu/Y substitution pattern at fixed composition, indicating that vibrational thermodynamics in this system are governed primarily by composition-averaged macroscopic quantities.

Overall, the results provide a comprehensive microscopic picture of how isovalent rare-earth substitution governs structural contraction, elastic stiffness, anisotropy, and lattice dynamics in LYSO solid solutions.

Supplementary Materials: The following supporting information can be downloaded at: https://www.mdpi.com/article/10.3390/cryst16060377/s1, Supplementary Information S1 contains the calculated elastic stiffness tensors (C_{ij}) for the considered YSO–LYSO–LSO compositions together with visualizations of the spatial dependence of Young's modulus, linear compressibility, shear modulus, and Poisson's ratio. Supplementary Information S2 provides a detailed description of the transformation between the 32-atom primitive unit cell used in the CRYSTAL calculations and the equivalent 64-atom conventional monoclinic unit cell in the B2/b setting. Supplementary Information S3 contains the total energies of all 76 symmetry-independent configurations considered in this work, together with vibrational free-energy contributions calculated for the energetically most favorable configurations.

Author Contributions: Conceptualization, A.P., A.I.P.; methodology, A.P., D.V.B.; validation, A.P., M.K., D.V.B.; formal analysis, A.P., D.V.B.; investigation, A.P., D.V.B.; resources, A.P., A.I.P.; data curation, A.P.; writing—original draft, D.V.B.; writing—review and editing, A.P.; M.K., D.V.B., A.I.P.; visualization, A.P., D.V.B.; project administration, M.K.; funding acquisition, A.I.P. All authors have read and agreed to the published version of the manuscript.

Funding: This research is supported by the Latvian State Research Program No. VPP-IZM-CERN-2022/1-0001 (AP, DB and AIP), while Marina Konuhova and Anatoli I. Popov were supported by Latvian research project lzp-2023/1-0453, "Prediction of long-term stability of functional materials under extreme radiation conditions".

Data Availability Statement: The original contributions presented in this study are included in the article/Supplementary Material. Further inquiries can be directed to the corresponding authors.

Conflicts of Interest: The authors declare no conflicts of interest.

References

1. Yanagida, T. Inorganic scintillating materials and scintillation detectors. *Proc. Jpn. Acad. B Phys. Biol. Sci.* **2018**, *94*, 75–97. [CrossRef]
2. Pepin, C.M.; Berard, P.; Perrot, A.L.; Houde, D.; Lecomte, R.; Melcher, C.L.; Dautet, H. Properties of LYSO and Recent LSO Scintillators for Phoswich PET Detectors. *IEEE Trans. Nucl. Sci.* **2004**, *51*, 789–795. [CrossRef]
3. Chen, J.; Zhang, L.; Zhu, R.Y. Large Size LSO and LYSO Crystal Scintillators for Future High-Energy Physics and Nuclear Physics Experiments. *Nucl. Instrum. Methods Phys. Res. A* **2007**, *572*, 218–224. [CrossRef]
4. Du, J.; Wang, Y.; Zhang, L.; Zhou, Z.; Xu, Z.; Wang, X. Physical Properties of LYSO Scintillator for NN-PET Detectors. In *Proceedings of the 2009 2nd International Conference on Biomedical Engineering and Informatics, Tianjin, China, 17–19 October 2009*; IEEE: New York, NY, USA, 2009; Volume 1, pp. 1–5. [CrossRef]
5. Yamamoto, S.; Okumura, S.; Kato, N.; Yeom, J.Y. Timing Measurements of Lutetium-Based Scintillators Combined with Silicon Photomultipliers for TOF-PET System. *J. Instrum.* **2015**, *10*, T09002. [CrossRef]
6. Mahani, H.; Taheri, A.; Askari, M. Detection Performance of Pixelated Lutetium–Yttrium Oxyorthosilicate (LYSO) Scintillators for High-Resolution Photon-Counting CT Imaging. *Rev. Sci. Instrum.* **2023**, *94*, 023308. [CrossRef] [PubMed]

7. Davi, F.; Rinaldi, D. Elastic Moduli and Optical Properties of LYSO Crystals: Theory and Experiments. *IEEE Trans. Nucl. Sci.* **2012**, *59*, 2106–2111. [CrossRef]
8. Saad, A.; Kocak, F.; Kirca, Z. The Impact of Crystal Length on Calorimeter Energy Resolution. *AIP Conf. Proc.* **2019**, *2178*, 030045. [CrossRef]
9. van der Sar, S.J.; Leibold, D.; Schaart, D.R. Experimental Investigation of the Potential of $LaBr_3$:Ce, LYSO:Ce, and YAP:Ce for Scintillator-Based X-Ray Photon-Counting Detectors. *Phys. Med. Biol.* **2026**, *71*, 025003. [CrossRef]
10. Lecoq, P.; Dafinei, I.; Auffray, E.; Schneegans, M.; Korzhik, M.V.; Missevitch, O.V.; Pavlenko, V.B.; Fedorov, A.A.; Annenkov, A.N.; Kostylev, V.L.; et al. Lead tungstate ($PbWO_4$) scintillators for LHC EM calorimetry. *Nucl. Instrum. Methods Phys. Res. A* **1995**, *365*, 291–298. [CrossRef]
11. Millers, D.; Grigorjeva, L.; Chernov, S.; Popov, A.; Lecoq, P.; Auffray, E. The temperature dependence of scintillation parameters in $PbWO_4$ crystals. *Phys. Status Solidi B* **1997**, *203*, 585–589. [CrossRef]
12. Korzhik, M.; Khrutchinsky, A.; Lecoq, P. The phenomenon of scintillation in solids. *Nucl. Instrum. Methods Phys. Res. A* **2002**, *486*, 381–384. [CrossRef]
13. Omelkov, S.I.; Nagirnyi, V.; Gundacker, S.; Spassky, D.A.; Auffray, E.; Lecoq, P.; Kirm, M. Scintillation yield of hot intraband luminescence. *J. Lumin.* **2018**, *198*, 260–271. [CrossRef]
14. Tamulaitis, G.; Auffray, E.; Gola, A.; Korzhik, M.; Mazzi, A.; Mechinski, V.; Nargelas, S.; Talochka, Y.; Vaitkevičius, A.; Vasil'ev, A. Improvement of the timing properties of Ce-doped oxyorthosilicate LYSO scintillating crystals. *J. Phys. Chem. Solids* **2020**, *139*, 109356. [CrossRef]
15. Nargelas, S.; Dosovitskiy, G.; Korzhik, M.; Tamulaitis, G. Role of inter- and intraconfigurational transitions of Pr^{3+} ion in nonequilibrium carrier relaxation in garnet-type scintillators. *Opt. Mater.* **2021**, *111*, 110676. [CrossRef]
16. Pankratov, V.; Popov, A.I.; Shirmane, L.; Kotlov, A.; Bizarri, G.A.; Burger, A.; Bhattacharya, P.; Tupitsyn, E.; Rowe, E.; Buliga, V.M.; et al. Luminescence and ultraviolet excitation spectroscopy of SrI_2 and SrI_2:Eu^{2+}. *Radiat. Meas.* **2013**, *56*, 13–17. [CrossRef]
17. Buryi, M.; Laguta, V.; Babin, V.; Laguta, O.; Brik, M.G.; Nikl, M. Rare-earth ions incorporation into $Lu_2Si_2O_7$ scintillator crystals: Electron paramagnetic resonance and luminescence study. *Opt. Mater.* **2020**, *106*, 109930. [CrossRef]
18. Buryi, M.; Bohacek, P.; Chernenko, K.; Krasnikov, A.; Laguta, V.V.; Mihokova, E.; Nikl, M.; Zazubovich, S. Luminescence and photo-thermally stimulated defect-creation processes in Bi^{3+}-doped single crystals of lead tungstate. *Phys. Status Solidi B* **2016**, *253*, 895–910. [CrossRef]
19. Kalinko, A.; Kotlov, A.; Kuzmin, A.; Pankratov, V.; Popov, A.; Shirmane, L. Electronic excitations in $ZnWO_4$ and $ZnxNi_{1-x}WO_4$ (x = 0.1–0.9) using VUV synchrotron radiation. *Cent. Eur. J. Phys.* **2011**, *9*, 432–437. [CrossRef]
20. Kimura, K.; Sharma, S.; Popov, A. Fast electron–hole plasma luminescence from track-cores in heavy-ion irradiated wide-band-gap crystals. *Nucl. Instrum. Methods Phys. Res. B* **2002**, *191*, 48–53. [CrossRef]
21. Auffray, E.; Borisevitch, A.; Gektin, A.; Gerasymov, I.; Korjik, M.; Kozlov, D.; Kurtsev, D.; Mechinsky, V.; Sidletskiy, O.; Zoueyski, R. Radiation damage effects in Y_2SiO_5:Ce scintillation crystals under γ-quanta and 24 GeV protons. *Nucl. Instrum. Methods Phys. Res. A Accel. Spectrom. Detect. Assoc. Equip.* **2015**, *783*, 117–120. [CrossRef]
22. Dormenev, V.; Brinkmann, K.; Kazlou, D.; Moritz, M.; Novotny, R.; Peter, M.; Zaunick, H. Scintillation Properties of Garnets and Oxyorthosilicates With Different Dopants. *IEEE Trans. Nucl. Sci.* **2023**, *70*, 1392–1397. [CrossRef]
23. Alva-Sánchez, H.; Zepeda-Barrios, A.; Díaz-Martínez, V.D.; Murrieta-Rodríguez, T.; Martínez-Dávalos, A.; Rodríguez-Villafuerte, M. Understanding the intrinsic radioactivity energy spectrum from ^{176}Lu in LYSO/LSO scintillation crystals. *Sci. Rep.* **2018**, *8*, 17310. [CrossRef]
24. Mao, R.; Wu, C.; Dai, L.; Lu, S. Crystal growth and scintillation properties of LSO and LYSO crystals. *J. Cryst. Growth* **2013**, *368*, 97–100. [CrossRef]
25. Cooke, D.W.; Mcclellan, K.; Bennett, B.; Roper, J.M.; Whittaker, M.; Muenchausen, R.; Sze, R. Crystal growth and optical characterization of cerium-doped $Lu_{1.8}Y_{0.2}SiO_5$. *J. Appl. Phys.* **2000**, *88*, 7360–7362. [CrossRef]
26. Kimble, T.; Chou, M.; Chai, B. Scintillation properties of LYSO crystals. *IEEE Nucl. Sci. Symp. Conf. Rec.* **2002**, *3*, 1434–1437. [CrossRef]
27. Mouhti, I.; Elanique, A.; Messous, M.Y.; Benahmed, A.; McFee, J.E.; Elgoub, Y.; Griffith, P. Characterization of CsI(Tl) and LYSO(Ce) Scintillator Detectors by Measurements and Monte Carlo Simulations. *Appl. Radiat. Isot.* **2019**, *154*, 108878. [CrossRef]
28. Pankratova, V.; Chernenko, K.; Bocharov, D.; Chesnokov, A.; Sychikova, Y.; Popov, A.I.; Pankratov, V. Unveiling of UV Intrinsic Luminescence in $(Lu,Y)_2SiO_5$:Ce^{3+} Single Crystals. *Opt. Mater.* **2024**, *152*, 115554. [CrossRef]
29. Pankratova, V.; Chernenko, K.; Popov, A.I.; Pankratov, V. Temperature Behavior of Ce^{3+} Emission in $(Lu,Y)_2SiO_5$ Single Crystals Excited by Vacuum Ultraviolet Synchrotron Light. *Opt. Mater. X* **2024**, *22*, 100322. [CrossRef]
30. Xu, K.; Hu, P.; Zhang, Q.; He, Q.; Liu, Q.; Wang, Y.; Huang, F.; Leng, J.; Lin, X.; Shi, Y.; et al. Annealing on Lattice Engineering and Luminescence in LYSO:Ce Scintillators. *CrystEngComm* **2026**, *28*, 1893–1904. [CrossRef]
31. Qiu, P.; Li, M.; Li, C.; Zhang, A.; Xue, Z.; Zheng, X.; Zhao, S.; Ding, D. Substantial Enhancement of Light Yield in LYSO:Ce Crystals via Trace Co^{2+} Co-Doping. *Chem. Eng. J.* **2026**, *529*, 172884. [CrossRef]

32. Campbell, C.; Rand, S.; Glodo, J.; Muller, M.; Wehe, D. Characterization of LuAG:Ce,Ca and LYSO:Ce,Ca Scintillators for Multiple Photon Emission. *Nucl. Technol.* **2026**, 1–8. [CrossRef]
33. Gioacchini, L.; Lega, A.; Nicolaidis, R.; Nozzoli, F. Characterization of the Light Response of LYSO Scintillator to Alpha Particles. *Nucl. Instrum. Methods Phys. Res. A* **2026**, *1084*, 171262. [CrossRef]
34. Speakman, S.A.; Porter, W.D.; Spurrier, M.A.; Melcher, C.L. Thermal expansion and stability of cerium-doped Lu_2SiO_5. *Mater. Res. Bull.* **2006**, *41*, 423–435. [CrossRef]
35. Sun, Z.; Wang, J.; Li, M.; Zhou, Y. Mechanical properties and damage tolerance of Y_2SiO_5. *J. Eur. Ceram.* **2008**, *28*, 2895–2901. [CrossRef]
36. Nowok, J.W.; Kay, J.P.; Kulas, R.J. Thermal expansion and high-temperature phase transformation of the yttrium silicate Y_2SiO_5. *J. Mater. Res.* **2001**, *16*, 2251–2255. [CrossRef]
37. Chen, J.; Zhang, L.; Zhu, R.Y. Large Size LYSO Crystals for Future High Energy Physics Experiments. *IEEE Trans. Nucl. Sci.* **2005**, *52*, 3133–3140. [CrossRef]
38. Mirzai, A.; Ahadi, A.; Melin, S.; Olsson, P. First-principle investigation of doping effects on mechanical and thermodynamic properties of Y_2SiO_5. *Mech. Mater.* **2021**, *154*, 103739. [CrossRef]
39. Tian, Z.; Sun, L.; Wang, J.; Wang, J. Theoretical prediction and experimental determination of the low lattice thermal conductivity of Lu_2SiO_5. *J. Eur. Ceram.* **2015**, *35*, 1923–1932. [CrossRef]
40. Tian, Z.; Zheng, L.; Wang, J.; Wan, P.; Li, J.; Wang, J. Theoretical and experimental determination of the major thermo-mechanical properties of RE_2SiO_5 (RE=Tb, Dy, Ho, Er, Tm, Yb, Lu, and Y) for environmental and thermal barrier coating applications. *J. Eur. Ceram.* **2016**, *36*, 189–202. [CrossRef]
41. Scalise, L.; Rinaldi, D.; Daví, F.; Paone, N. Measurement of ultimate tensile strength and Young modulus in LYSO scintillating crystals. *Nucl. Instrum. Methods Phys. Res. A Accel. Spectrom. Detect. Assoc. Equip.* **2011**, *654*, 122–126. [CrossRef]
42. Xie, S.; Sun, Q.; Ying, G.; Guo, L.; Huang, Q.; Peng, Q.; Xu, J. Ultra-precise surface processing of LYSO scintillator crystals for Positron Emission Tomography. *Appl. Surf. Sci.* **2019**, *469*, 573–581. [CrossRef] [PubMed]
43. Wang, J.; Tian, S.; Li, G.; Liao, F.; Jing, X. Preparation and X-ray characterization of low-temperature phases of R_2SiO_5 (R = rare earth elements). *Mater. Res. Bull.* **2001**, *36*, 1855–1861. [CrossRef]
44. Ghosh, P.; Sadhu, S.; Patra, A. Preparation and photoluminescence properties of Y_2SiO_5:Eu^{3+} nanocrystals. *Phys. Chem. Chem. Phys.* **2006**, *8*, 3342–3348. [CrossRef] [PubMed]
45. Mock, A.; Korlacki, R.; Knight, S.; Schubert, M. Anisotropy and phonon modes from analysis of the dielectric function tensor and the inverse dielectric function tensor of monoclinic yttrium orthosilicate. *Phys. Rev. B* **2018**, *97*, 165203. [CrossRef]
46. Dramićanin, M.D.; Viana, B.; Andrić, Z.; Djokovic, V.; Luyt, A.S. Synthesis of Y_2SiO_5:Eu^{3+} nanoparticles from a hydrothermally prepared silica sol. *J. Alloys Compd.* **2008**, *464*, 357–360. [CrossRef]
47. Mighell, A.D. Conventional Cells—The Last Step Toward General Acceptance of Standard Conventional Cells for the Reporting of Crystallographic Data. *J. Res. Natl. Inst. Stand. Technol.* **2002**, *107*, 373–377. [CrossRef] [PubMed]
48. Michel, C.; Buisson, G.; Bertaut, E.F. Structure de Y_2SiO_5. *Comptes Rendus Hebd. Seances l'Acad. Sci. Ser. B* **1967**, *264*, 397–399.
49. Villars, P.; Cenzual, K. X2-Y_2SiO_5 Crystal Structure: Datasheet from "Pauling File Multinaries Edition—2012". In *SpringerMaterials*; Springer: Berlin/Heidelberg, Germany, 2016.
50. O'Bryan, H.M.; Gallagher, P.K.; Berkstresser, G. Thermal Expansion of Y_2SiO_5 Single Crystals. *J. Am. Ceram. Soc.* **1988**, *71*. [CrossRef]
51. Maksimov, B.; Ilyukhin, V.; Kharitonov, Y.; Belov, N. Crystal structure of yttrium oxyorthosilicate $Y_2O_3SiO_2$ and Y_2SiO_5. Dual function of yttrium. *Kristallografiya* **1970**, *15*, 926–933.
52. Zheng, L.; Zhao, G.; Yan, C.; Xu, X.; Su, L.; Dong, Y.; Xu, J. Raman spectroscopic investigation of pure and ytterbium-doped rare earth silicate crystals. *J. Raman Spectrosc.* **2007**, *38*, 1421–1428. [CrossRef]
53. Denault, K.A.; Brgoch, J.; Kloß, S.D.; Gaultois, M.W.; Siewenie, J.; Page, K.; Seshadri, R. Average and Local Structure, Debye Temperature, and Structural Rigidity in Some Oxide Compounds Related to Phosphor Hosts. *ACS Appl. Mater. Interfaces* **2015**, *7*, 7264–7272. [CrossRef]
54. Ding, D.; Weng, L.; Yang, J.; Ren, G.; Wu, Y. Influence of yttrium content on the location of rare earth ions in LYSO:Ce crystals. *J. Solid State Chem.* **2014**, *209*, 56–62. [CrossRef]
55. Chiriu, D.; Faedda, N.; Lehmann, A.G.; Ricci, P.C.; Anedda, A.; Desgreniers, S.; Fortin, E. Structural characterization of $Lu_{1.8}Y_{0.2}SiO_5$ crystals. *Phys. Rev. B* **2007**, *76*, 054112. [CrossRef]
56. Mengucci, P.; André, G.; Auffray, E.; Barucca, G.; Cecchi, C.; Chipaux, R.; Cousson, A.; Daví, F.; Vara, N.D.; Rinaldi, D.; et al. Structural, mechanical and light yield characterisation of heat treated LYSO:Ce single crystals for medical imaging applications. *Nucl. Instrum. Methods Phys. Res. A Accel. Spectrom. Detect. Assoc. Equip.* **2015**, *785*, 110–116. [CrossRef]
57. Gustafsson, T.; Klintenberg, M.; Derenzo, S.E.; Weber, M.J.; Thomas, J.O. Lu_2SiO_5 by single-crystal X-ray and neutron diffraction. *Acta Crystallogr. C* **2001**, *57*, 668–669. [CrossRef] [PubMed]

58. Anan'eva, G.V.; Korovkin, A.M.; Merkulyaeva, T.I.; Morozova, A.M.; Petrov, M.V.; Savinova, I.R.; Startsev, V.R.; Feofilov, P.P. Growth of lanthanide oxyorthosilicate single crystals, and their structural and optical characteristics. *Izv. Akad. Nauk SSSR Neorg. Mater.* **1981**, *17*, 754–758.
59. Felsche, J. The crystal chemistry of the rare-earth silicates. In *Rare Earths*; Springer: Berlin/Heidelberg, Germany, 1973; pp. 99–197.
60. Cong, H.; Zhang, H.; Wang, J.; Yu, W.; Fan, J.; Cheng, X.; Sun, S.; Zhang, J.; Lu, Q.; Jiang, C.; et al. Structural and thermal properties of the monoclinic Lu_2SiO_5 single crystal: Evaluation as a new laser matrix. *J. Appl. Crystallogr.* **2009**, *42*, 284–294. [CrossRef]
61. Stokey, M.; Mock, A.; Korlacki, R.; Knight, S.; Darakchieva, V.; Schöche, S.; Schubert, M. Infrared active phonons in monoclinic lutetium oxyorthosilicate. *J. Appl. Phys.* **2020**, *127*, 115702. [CrossRef]
62. Bennett, D.W. *Understanding Single-Crystal X-Ray Crystallography*; Wiley-VCH Verlag GmbH & Co. KGaA: Weinheim, Germany, 2010.
63. Wagner, N.; Hartman, M.T.; Fang, B.; Dickmann, J.; Kroker, S. Temperature-dependent mechanical losses of Eu^{3+}:Y_2SiO_5 for spectral hole burning laser stabilization. *APL Mater.* **2025**, *13*, 061107. [CrossRef]
64. Tian, Z.; Sun, L.; Zheng, L.; Wang, J.; Li, J.; Hu, Z. In situ hot pressing/reaction synthesis, mechanical and thermal properties of Lu_2SiO_5. *J. Eur. Ceram. Soc.* **2014**, *34*, 4403–4409. [CrossRef]
65. Jang, B.; Feng, F.; Lee, K.S.; García, E.; Nistal, A.; Nagashima, N.; Kim, S.; Oh, Y.; Kim, H. Thermal behavior and mechanical properties of Y_2SiO_5 environmental barrier coatings after isothermal heat treatment. *Surf. Coat. Technol.* **2016**, *308*, 24–30. [CrossRef]
66. Erba, A.; Desmarais, J.K.; Casassa, S.; Civalleri, B.; Donà, L.; Bush, I.J.; Searle, B.; Maschio, L.; Edith-Daga, L.; Cossard, A.; et al. CRYSTAL23: A Program for Computational Solid State Physics and Chemistry. *J. Chem. Theory Comput.* **2022**, *19*, 6891–6932. [CrossRef]
67. Perdew, J.P.; Wang, Y. Accurate and simple analytic representation of the electron-gas correlation energy. *Phys. Rev. B* **1992**, *45*, 13244–13249. [CrossRef]
68. Oliveira, D.V.; Laun, J.; Peintinger, M.F.; Bredow, T. BSSE-correction scheme for consistent gaussian basis sets of double- and triple-zeta valence with polarization quality for solid-state calculations. *J. Comput. Chem.* **2019**, *40*, 2364–2376. [CrossRef]
69. Perger, W.; Criswell, J.; Civalleri, B.; Dovesi, R. *Ab-initio* calculation of elastic constants of crystalline systems with the CRYSTAL code. *Comput. Phys. Commun.* **2009**, *180*, 1753–1759. [CrossRef]
70. Erba, A.; Mahmoud, A.; Orlando, R.; Dovesi, R. Elastic properties of six silicate garnet end members from accurate *ab initio* simulations. *Phys. Chem. Miner.* **2013**, *41*, 151–160. [CrossRef]
71. Mustapha, S.; D'Arco, P.; Pierre, M.D.L.; Noël, Y.; Ferrabone, M.; Dovesi, R. On the use of symmetry in configurational analysis for the simulation of disordered solids. *J. Phys. Condens. Matter* **2013**, *25*, 105401. [CrossRef] [PubMed]
72. D'Arco, P.; Mustapha, S.; Ferrabone, M.; Noël, Y.; Pierre, M.D.L.; Dovesi, R. Symmetry and random sampling of symmetry independent configurations for the simulation of disordered solids. *J. Phys. Condens. Matter* **2013**, *25*, 355401. [CrossRef] [PubMed]
73. Monkhorst, H.J.; Pack, J.D. Special points for Brillouin-zone integrations. *Phys. Rev. B* **1976**, *13*, 5188–5192. [CrossRef]
74. Gaillac, R.; Pullumbi, P.; Coudert, F.X. ELATE: An open-source online application for analysis and visualization of elastic tensors. *J. Condens. Matter Phys.* **2016**, *28*, 275201. [CrossRef]
75. Hill, R. The Elastic Behaviour of a Crystalline Aggregate. *Proc. Phys. Soc. A* **1952**, *65*, 349. [CrossRef]
76. Honorio, T.; Carasek, H.; Cascudo, O. Friedel's salt: Temperature dependence of thermoelastic properties. *Cem. Concr. Res.* **2022**, *160*, 106904. [CrossRef]
77. Yan, J.; Shou, H.; Peng, M.; Duan, Y.; Cao, Y. The anisotropic properties and Debye temperatures of Ti-Zn compounds: A first-principles calculation. *Mater. Res. Express.* **2019**, *6*, 116528. [CrossRef]
78. Rusevich, L.L.; Brik, M.G.; Gryaznov, D.; Srivastava, A.M.; Chervyakov, I.; Zvejnieks, G.; Bocharov, D.; Kotomin, E.A. First-Principles Linear Combination of Atomic Orbitals Calculations of K_2SiF_6 Crystal: Structural, Electronic, Elastic, Vibrational and Dielectric Properties. *Materials* **2024**, *17*, 4865. [CrossRef]
79. Subhoni, M.; Zafari, U.; Ma, C.G.; Srivastava, A.M.; Beers, W.W.; Cohen, W.E.; Brik, M.G.; Piasecki, M.; Yamamoto, T. Influence of Isostatic Pressure on the Elastic and Electronic Properties of K_2SiF_6:Mn^{4+}. *Materials* **2022**, *15*, 613. [CrossRef] [PubMed]
80. Anderson, O.L. A simplified method for calculating the Debye temperature from elastic constants. *J. Phys. Chem. Solids* **1963**, *24*, 909–917. [CrossRef]
81. Suzuki, H.; Tombrello, T.A.; Melcher, C.L.; Schweitzer, J.S. UV and gamma-ray excited luminescence of cerium-doped rare-earth oxyorthosilicates. *Nucl. Instrum. Methods Phys. Res. A* **1992**, *320*, 263–272. [CrossRef]
82. Mechnich, P. Y_2SiO_5 coatings fabricated by RF magnetron sputtering. *Surf. Coat. Technol.* **2013**, *237*, 88–94. [CrossRef]
83. Melcher, C.L.; Schweitzer, J.S. Cerium-doped lutetium oxyorthosilicate: A fast, efficient new scintillator. *IEEE Trans. Nucl. Sci.* **1992**, *39*, 502–505. [CrossRef]

84. Daghighian, F.; Shenderov, P.; Pentlow, K.S.; Graham, M.C.; Eshaghian, B.; Melcher, C.L.; Schweitzer, J.S. Evaluation of cerium doped lutetium oxyorthosilicate (LSO) scintillation crystal for PET. *IEEE Trans. Nucl. Sci.* **1993**, *40*, 1045–1047. [CrossRef]
85. Ching, W.Y.; Ouyang, L.; Xu, Y.N. Electronic and optical properties of Y_2SiO_5 and $Y_2Si_2O_7$ with comparisons to a-SiO_2 and Y_2O_3. *Phys. Rev. B* **2003**, *67*, 245108. [CrossRef]

Disclaimer/Publisher's Note: The statements, opinions and data contained in all publications are solely those of the individual author(s) and contributor(s) and not of MDPI and/or the editor(s). MDPI and/or the editor(s) disclaim responsibility for any injury to people or property resulting from any ideas, methods, instructions or products referred to in the content.